Investigation Of The Structural Analysis and Design of Cable-Stayed Bridge with Trusses

Ahmad Samadi , Engineering Building & Infrastructure, contact@ebni.com.au
Dep. of Civil and Environmental Engineering, Western Sydney University, Sydney, NSW, 2000. 12/05/2025.

Abstract

Following the building of the first contemporary cable-stayed bridge, the Swedish Stromsund Bridge, in 1955, structural engineers began to take an interest in the idea and real-world uses of cable-stayed bridges. Cable-stayed bridges are more rigid and use less material than suspension bridges, particularly for the stay cables and abutments. Cable-stayed bridges with main span lengths greater than 1000 meters are entering a new era thanks to recent developments in design and construction techniques as well as the availability of high-strength steel cables (Hassan 2010) Cable-stayed bridges represent a major innovation in long-span bridge engineering, offering efficiency, aesthetic appeal, and structural resilience. This paper explores the design principles, mechanical behavior, material properties, and optimization methods involved in the development and analysis of cable-stayed bridges. Special attention is given to stay cable configurations, post-tensioning strategies, anchorage systems, and advanced failure analyses including non-linear and pushover techniques. A comprehensive literature review, analytical modeling, and practical design recommendations are provided to support future bridge truss system design and safety.

Components and types of cable stayed bridges

The most prevalent configurations for stay cables are the harp, fan, and semi-fan arrangements, as illustrated in Fig. 1 (Anon n.d.). For bridges with extensive spans, the harp layout is generally considered less appropriate, as it necessitates a higher pylon and generates substantial forces within the stay cables. The fan pattern, while suitable for moderate spans with fewer stay cables, becomes problematic for larger structures due to the increased weight of anchorages and difficulties in accommodating them as the number of cables grows. The semi-fan pattern emerges as the optimal choice, offering a middle ground between the harp and fan designs. By combining the strengths and mitigating the weaknesses of both arrangements, the semi-fan pattern has been widely adopted in contemporary cable-stayed bridges. A prime example is the Sutong Bridge in China, which boasts the world's longest cable-stayed main span at 1088 m.

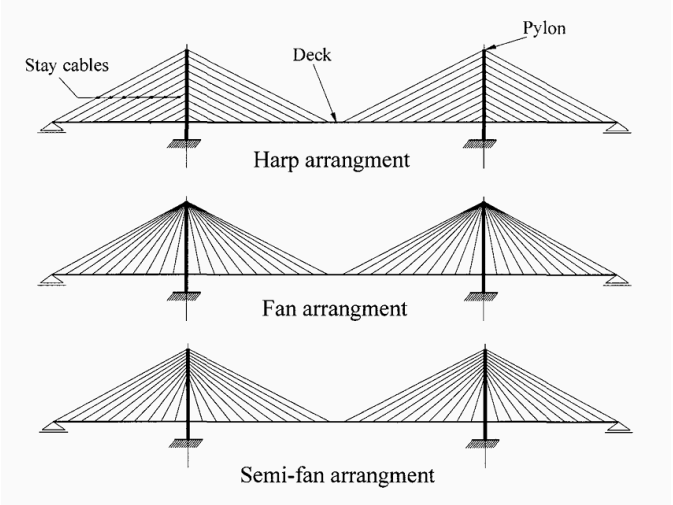

Figure 1: Different component of cable stayed bridge

The composite steel-concrete deck is a widely adopted system in cable-stayed bridge design and construction. This configuration features a deck comprising two structural steel edge girders linked by transverse steel floor beams, which support a precast reinforced concrete slab, as illustrated in Figure 2. The benefits of these composite decks include:

1. Cost-effectiveness of the concrete roadway slab compared to steel orthotropic decks.
2. Reduced redistribution of compression forces onto steel girders due to shrinkage and creep, achieved through the use of precast slabs.
3. Enhanced rotational resistance attained by anchoring stay cables to the exterior steel main girders.
4. Ease of construction for the relatively lightweight steel girders prior to the addition of the heavier concrete slab.
5. Significantly lower dead weight compared to a full concrete deck.

Consequently, composite decks have been employed in numerous cable-stayed bridges worldwide, such as the Quincy Bayview Bridge in the USA, Annacis Island Bridge in Canada, and Qingzhou Bridge in China (Sung et al. 2006)and (Ren & Peng 2005).

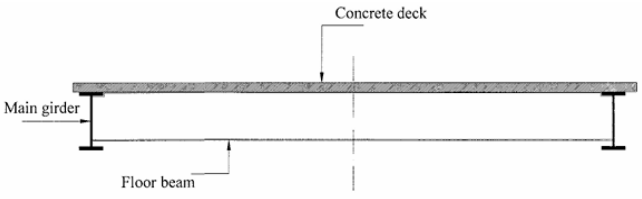

Figure 3: Illustration of bridge deck

Cable-stayed bridges employ inclined stay cables that are post-tensioned to counteract the deck's dead load. This post-tensioning is applied to minimise both vertical deck deflection and lateral pylon deflection along the bridge's longitudinal axis. The combined effect of dead and post-tensioning cable forces results in a deck bending moment equivalent to that of a beam on continuous rigid supports at cable-deck connections, while pylons function as pure axial members. Post-tensioning cable forces influence internal force distribution and overall bridge design, making them a crucial design parameter for effective bridge construction.

Determining the optimal distribution of post-tensioning cable forces is considered one of the most challenging aspects of cable-stayed bridge design. The trend towards longer span bridges necessitates a greater number of stay cables, increasing bridge redundancy and complicating the optimisation process (Lee et al. 2008). From a mathematical perspective, the problem of evaluating optimal post-tensioning cable forces may not yield a unique solution (Sung et al. 2006).

Four methods have been developed to determine post-tensioning cable forces in cable-stayed bridges. These approaches aim to either minimise vertical deck deflections to a convergence tolerance or achieve a bending moment diagram along the deck as if it were supported on simple rigid supports at cable locations. (Wang et al. 1993) proposed the zero displacement method to determine post-tensioning cable forces and the initial bridge profile under dead load. This iterative process begins by assuming zero tension in stay cables and seeks an equilibrium position with zero deck deflections. Although the initial configuration satisfies equilibrium conditions, it does not result in zero deflections. Therefore, the process is repeated using the previously determined cable forces as initial values until the convergence tolerance is achieved at selected deck locations. However, this method is known for slow convergence and requires significant computational effort (Kim & Lee 2001).

Types of post tensioning cables stay

In general, the stay cables' steel composition is different from structural steel because it has a higher carbon content. Although structural steel has a carbon content of 0.15 to 0.20%, (Gimsing & Georgakis 2011) found that the material utilized to make the stay cables had a carbon concentration of 0.80%. The stay cable material has a tensile strength of roughly 1800 MPA, which is roughly four times that of mild structural steel (370 MPA), due to its increased carbon content. Additionally, it has a tensile strength of 790 MPA, which is more than twice as strong as that of structural steel.

The stay cable material's tensile strength, which is roughly 1800 MPA, is nearly four times that of mild structural steel (370 MPA) because of its increased carbon content. Additionally, its tensile strength (= 790 MPA) is more than double that of the high strength structural steel. A discernible reduction in ductility compensates for the gain in tensile strength. The stay cable material has an elongation of 4% at the breaking point. The elongation at the breaking point of mild structural steel and high strength structural steel can reach values of 24% and 18%, respectively(Gimsing & Georgakis 2011).
The types of cables usually used for cable supported bridges are: a- Parallel-bar cables. b- Locked coil strand cables. c- Parallel-wire cables. d- Parallel strand cables.

a. Parallel bar cables

Steel threaded parallel-bar cables (fig. 2.1) are typically available in sizes of 16, 19, 25, 32, 36, 43, and 57mm. (Walther et al. 1999) reported that bars with widths up to 16mm are delivered in reels, whereas those larger than 16mm are delivered in straight lengths of 15 or 20m. To maintain bar continuity with diameters over 16mm, use couplers. These cables have an elastic modulus of 210000 N/mm^2 and an ultimate strength range of 1030-1470 N/mm^2. Stay cables manufactured from stressed bars have a bigger cross section due to their lower ultimate strength compared to other wires utilized in their fabrication. However, larger cross sections reduce stress fluctuations and improve stay cable fatigue strength. Refer to figure 4 for stressing bars mounted in metal ducts, held in place by polyethylene spacers and parallel to each other. The longitudinal sliding of the bars allows for individual straining of the steel bars. Cement grout is typically injected into the voids inside metal ducts around steel bars after tensioning all bars. The cement grout injection protects steel bars from corrosion and helps bear some live loads.

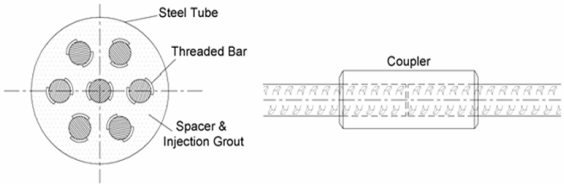

Figure 4: Parallel bar cables (Walther et al. 1999)

b. Locked coil strand cables

A variety of wire cross sections are employed in the locked coil strand to create a strand with a sleeker and more compact surface. The locked coil strand will typically consist of a nucleus of a standard helical strand, which is composed of round wires. The core is surrounded by one to several layers of wedge-shaped wires, while the peripheral layers are composed of wires with a unique S-shape figure 5. The S-shape layer creates an envelope that is somewhat water-tight, which is why they are referred to as "Locked Coil Cables" . These strands are produced by rotating successive wire layers in a manner that is generally in opposition to the direction of the helix. The stiffness of the multi-wire strands decreases more than that of the seven wire strands due to the reduced pitch. The nominal elastic modulus of the multiwire helical strand is approximately 15-25% lower than that of straight

wires (Gimsing & Georgakis 2011). Typically, the elastic modulus of these types of filaments is 170,000 N/mm^2. The elongation of a helical strand will be a result of the elastic strain in the wires and an irreversible elongation caused by the strand's compaction when the initial loading is applied. In order to eliminate this non-elastic elongation, a pre-stressing procedure is implemented to ensure that the strand behaves in a nearly ideal elastic manner in the final structure. The diameters of the secured coil strands typically range from 30mm to 150mm. The greatest diameters of locked coil strands are employed in cable-stayed bridges, where a stay cable may consist of a single strand. In situations where the ultimate cable is composed of multiple strands, the smaller diameters (60 to 80mm) are employed. In contrast to other types of stay cables, stay cables with locked coil strands are installed without external conduits or grouting. Consequently, they must be fabricated with extreme care to ensure the corrosion protection of all of their wires.

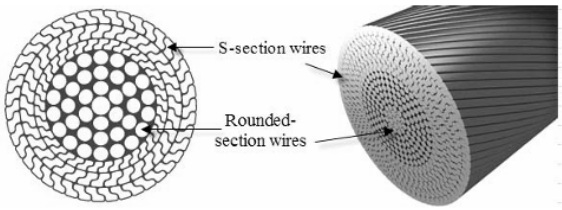

Figure 5: Locked coil strand

c. Parallel wire cables

They are clusters of 7mm wires see figure: . The number of wires in each bundle varies from 50 to 350. The utmost strength of the wires in these cables is 1670 N/mm^2. This suggests that a single wire can sustain 6.5 tons, whereas a bundle of 300 wires can support 1950 tons.
The elastic modulus of these cables is approximately 205,000 N/mm^2, which is marginally lower than that of parallel bar cables. Stay cables with parallel wires have been found to be capable of withstanding stress variations of 350-400 N/mm^2 over 2 million cycles, with a maximum stress of 750 N/mm^2, which is equivalent to 45% of the cable's complete length before it is delivered to the erection site. The utmost projected load for the life of a stay cable is typically 1.5 times the test jacking load.

d. Parallel strand cables

They are made up of groups of strands. The strand typically consists of seven 5mm wires. These strands are easiest to find in cable-supported bridges. They are currently commonly employed as tendons in prestressed concrete buildings. The seven-wire strand has a 5mm wire core and a layer of six wires, with a nominal diameter of 15mm and a cross sectional area of 150 mm^2 (see figure 4). Each of the six wires encircling the core wire has the same pitch and helix direction. A large pitch results in a modest inclination of the wire axis relative to the strand axis. The rigidity of the seven-wire strand is comparable to that of straight wires. The nominal elastic modulus of a seven-wire strand is typically 5-6% lower than that of wires. These cables typically have an elastic modulus of 195000 N/mm^2 (Gimsing & Georgakis 2011). According to international norms and requirements, stay cable systems should be tested for fatigue strength.

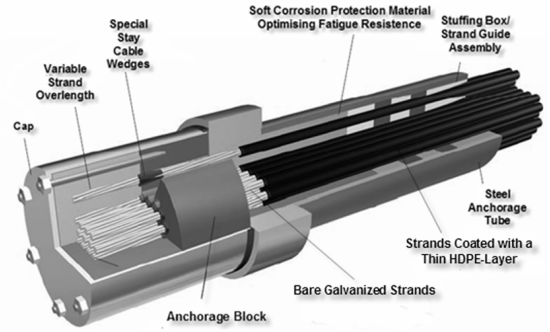

Figure 5: Anchorage components of parallel strand stay cable

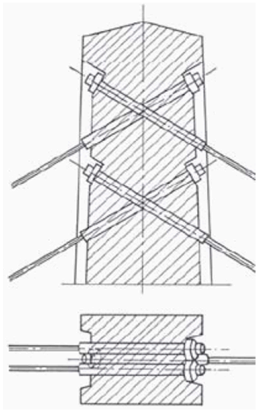

Figure 6: Isotension schematic diagram of anchors behind concrete(Leonhardt & Zellner 1980).

Existing post-tensioning optimisation techniques typically focus on achieving one of two outcomes. The first involves restricting the bridge deck's vertical deflections to a specified tolerance value. The second aims to produce a bending moment diagram along the deck that simulates the deck resting on simple rigid supports at cable points. However, attaining these desired deck conditions may sometimes result in either excessive bending moments in the pylons, surpassing imposed limits, or disproportionately large cable forces. Consequently, there is a pressing need to incorporate pylon behaviour into the optimisation process. The current method's objective function simultaneously minimises transverse deflections of both the deck and pylon tops. This approach leads to a reduction in bending moment distributions along both the deck and the pylon.

Ratio between side span and main span length

The structural system's overall stability is primarily guaranteed by the backstays of contemporary cable-stayed bridges. In the event that the main span is under active load, they assist in stabilizing the tower's tip by relocating it toward the side span. The backstay

forces are increased by the active load q on the main span (see figure 7). The backstay forces are reduced to their minimum level when the live load q occupies only the side span (see figure 7). In comparison to all other cables, the backstays typically experience the most significant tension variations/amplitudes. Their dimensions must be designed to ensure that the aforementioned stress variations are safely contained below their fatigue strength.
The following equations can be derived by disregarding the bending stiffness of the deck and presuming that all stay cables intersect at the top of the tower head, as shown in figure 7 (Gimsing & Georgakis 2011)

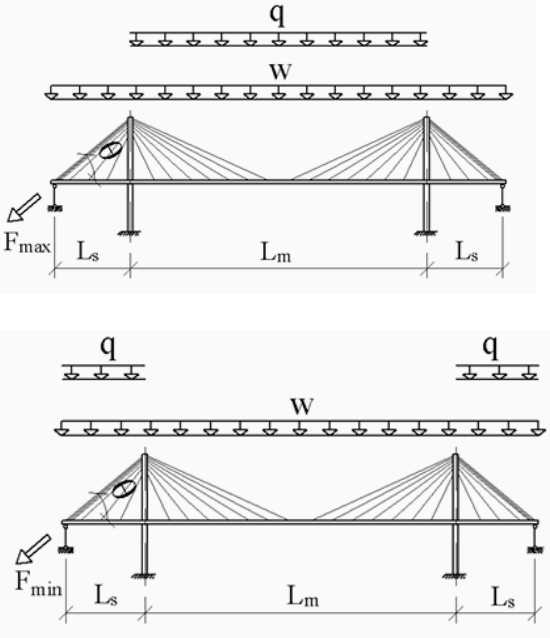

Figure 7: Load case for maximum and minimum back stay forces

(1) $F_{max} L_s sin(\theta) = (q + w)\frac{(\frac{L_m}{2})^2}{2} - w\frac{L_s^2}{2}$

(2) $F_{min} L_s sin(\theta) = w\frac{(\frac{L_m}{2})^2}{2} - (q + w)\frac{L_s^2}{2}$

$\frac{(1)}{(2)} = \zeta = \frac{F_{min}}{F_{max}} = \frac{wL_m^2 - 4(w+q)L_s^2}{(w+q)L_m^2 - 4wL_s^2}$, $\lambda = \frac{q}{w}$, $\eta = \frac{L_s}{L_m}$

(3) $\eta = \frac{1-4(1+\lambda)\eta^2}{(1+\lambda)-4\eta^2}$

(5) $\eta = \frac{1}{2}\sqrt{\frac{\zeta(1+\lambda)-1}{\zeta-1-\lambda}} = \frac{1}{2}\sqrt{\frac{1-\zeta(1+\lambda)}{1-\zeta+\lambda}}$

$F_{max} = Maximum\ back\ stayed\ force$ $L_s = Partial\ length\ of\ seck$

$L_m = Main\ span\ length$

$\eta = ratio\ between\ side\ span\ length\ and\ main\ span\ length$,

$\theta = angle\ of\ stay\ cable$

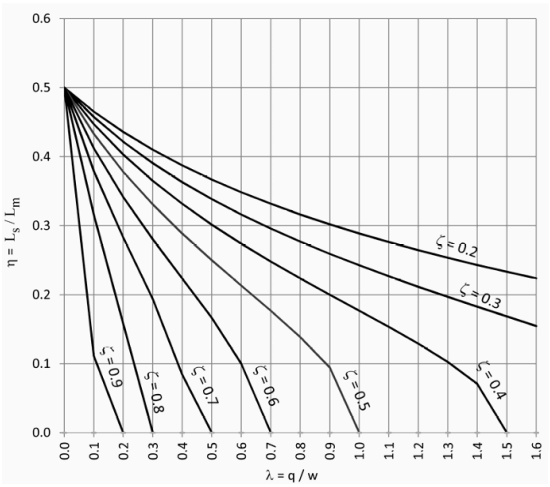

Figure 8: Relationship between the live load and the dead load and the ratio of the lateral span to the main span (Gimsing & Georgakis 2011).

Stiffness of stay cables

Under dead load, stay cables are catenary. Stay cables sag under dead load, resulting in a lower effective elastic modulus E_{eff} than the steel material E_0. For cables represented as straight elements in a computer model, employ a modulus of elasticity $E_{eff} < E_0$, especially for lengthy cables (see to figure 8). E_{eff} is affected by cable length, force, and self-weight. The (Chambers and Ernst 2005) formula can be used to compute the effective elastic modulus E_{eff}.

(6) $E_{eff} = E_0 \frac{1}{1+\frac{\gamma^2 L_h^2 E_0}{12\sigma^3}}$

$E_{eff} = effective\ elastic\ modulus\ (N/mm^2)$

$E_0 = elastic\ modulus\ of\ the\ stay\ cable\ in\ absence\ of\ sag\ effect\ (N/mm^2)$

$\gamma = the\ specific\ weight\ of\ the\ stay\ cable\ material\ in\ (N/mm^3)$

$L_h = the\ projected\ stay\ cable\ length\ in\ plan\ (mm)$

$\sigma = the\ axial\ stress\ of\ the\ cable\ (N/mm^2)$

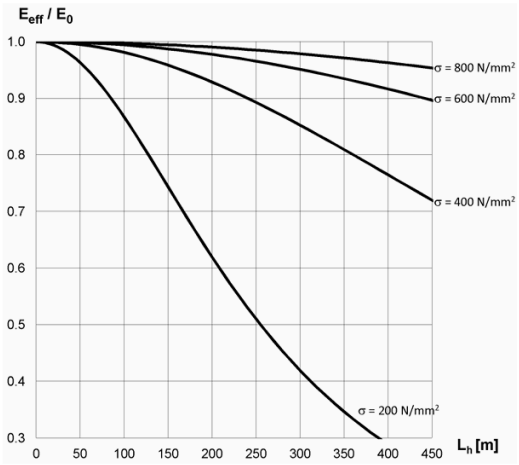

Figure 8: Effect of the stay cable sag on its elastic modulus (Gimsing and Georgakis 2011)

Different structural supporting systems bridge components.

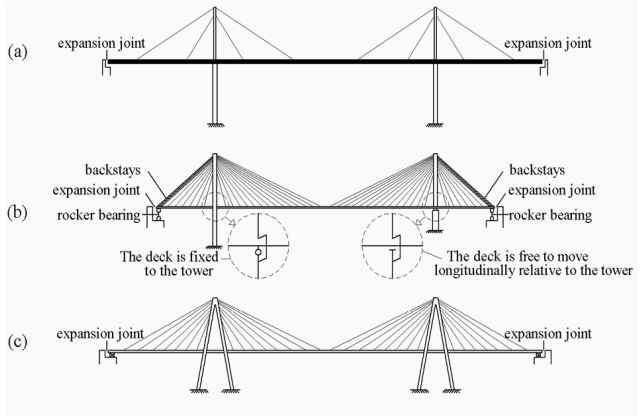

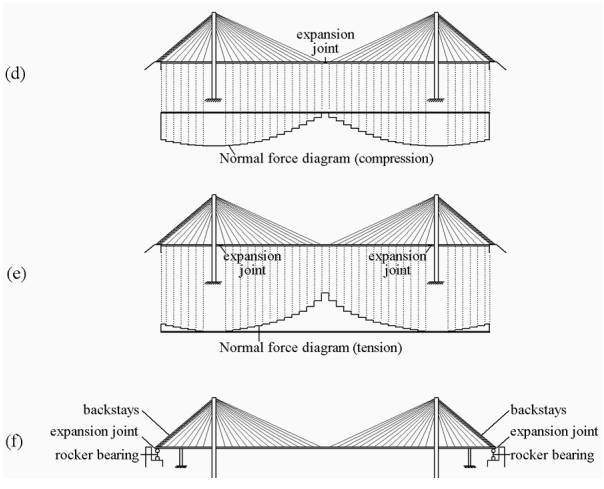

Figure 9: Figure showing different structural supporting systems of cable stayed bridges and back stayed bridges.

The supporting system impacts how towers, stay cables, and decks in a normal cable-stayed bridge support self-weight and external loads. Cable-stayed bridges are shown in Figure 9. Cable-stayed bridges originally had a few stay cables supporting a rigid deck . Only thin towers above the deck level are needed to support the vertical component pressures from the few stay cables and minimal bending moments (Leonhardt & Zellner 1980). Figure 9 (a) lacks backstays to connect the tower tip to the rigid end support.

The narrow deck and back stays of the bridge in figure 9 (b) connect the tower apex to the stiff end supports, which longitudinally stabilize the towers. Rocker bearings' upper ends are hinged to the deck. All hinge at the bottom.

These rocker bearings support backstay vertical forces and deck horizontal movement. A horizontal element This structure balances horizontal stay forces on the main span side by supporting the back stays on the deck. Temperature, shrinkage, creep, and live loads shift the deck longitudinally. As the deck moves at its top ends, rocker bearings spin around their bottom hinges. Match rocker bearing height to motion magnitude to avoid deck-bearing restrictions.

The bridge in figure 9 (c) features firm towers. Not like the bridge in figure 9 (b), this tower does not need back-stays. The bridge in figure 9 (d) features an extension joint in the center of its main span, unlike others. The bridge deck is linked to terminal supports, although backstays are external. (e) illustrates a bridge with a supporting system like (d), but the deck has two expansion joints near the towers. Figures 9 (b) and (c) show a bridge deck that can move longitudinally or be securely attached to one tower. If the side spans are short and/or the towers are flexible and tall, figures 9 (d) and (e) bridge decks can only be joined longitudinally. Avoiding high tower-deck restraining pressures requires this strategy. Under dead load, bridge decks in figures 9 (a) to (d) experience compression normal forces, while deck (e) experiences tension normal pressures. Steel decks work best for figure 9(e). (Hassan 2010) cite F. de Miranda's Arno bridge design.

Analysis of mechanical behaviour of cable-stayed bridge.

Mathematical background

A mathematical model for the deformed structure's shape is the basis of the observed cable-stayed bridge analysis method. The equations show how element strains affect deformations. Forces acting on the stiffening girder (e.g., support reactions, cable tension forces, dead load, varying loads) are sensed separately, but the entire system state is determined via superposition (Straupe & Paeglitis 2012).For a statically unknown beam, the differential equation (1) of the deformed axle shape is solved using unknown reaction forces at the elastic support points:

$$(1)\ E_s I y''(x) = M(x) \qquad where:\ y(x) = axle\ equation\ deformations,$$
$$M(x) = Bending\ moment\ of\ the\ beam$$

(2) $P = [M_{P0}(d,x)^{-1}].[-M_{req}(x) - M_d(x)]$

Where $M_{req}(x)$ = *optimal bending moment peak to be defined*

$M_{P0}(d,x)$ = Bending moment diagram caused by unit force at a distance d $M_d(x)$ = Bending moment diagram due to dead load P_0 = point load.

System geometry:

Describing the bridge segmentation for back stayed bridge.

A cable-stayed bridge with three symmetrical spans will be seen. While the back span (80 m) is divided into 8 panels, the central span (260 m) is divided into 21 panels. Thus, each pylon supports ten cables for the central span, but only seven cables support the back-spans (see Figure 10). Anchoring the three cables that are still in this example to the large supports that are located at the extremities of the bridge will be done. The pylon is supposed to be balanced, and these three wires are supposed to accomplish such. The cables are fully regulated (pre-stressed) to obtain the desired deformed shape of the stiffening girder.

Role of cables in stiffening girder

Before (Straupe & Paeglitis 2011), the optimal division of girders into panels is addressed. The same task has been resolved for any arbitrary panel length, and the requisite cable tensile forces have been determined to ensure that the utmost positive and negative bending moments within each individual panel are the same absolute value.

The number of cables in each span is one less than the number of panels. In the combined model, the equation system for optimal cable forces (i.e. elastic support responses) has more unknowns than equations (Kachurin et al. 1971). The goal of minimizing the bending moment value of a stiffening girder at rigid supports (pylons) is not an appropriate approach. Tendons should be used to prestress these regions in order to mitigate the tensile tensions. In practice, this solution is typically required for the cantilever construction method.

The system of equations is solved to determine the necessary cable tensile forces. The bending moment diagram of the strengthening girder from cable tension forces is depicted in Figure 10, which is the most suitable for the bridge's observed system. The height of the pylons is selected to ensure that the inclination angle of the longest cable is 25°.

In order to compare the tensile forces in cables, as well as the axial forces and compressive tensions in the girder of different system modifications, it is necessary to make the aforementioned assumptions (Juozapaitis & Norkus 2007). Two methods of erection of the stiffening girder are observed: the first involves the use of temporary supports, which are then used to add cable forces after the entire girder is joined (Lozano-Galant et al. 2012). The second method involves the use of cantilevers, which are used to add cables in a progressive manner.

It is important to mention that the first option generates an axial tensile force in the girder during the middle portion of the central span. However, the second option eliminates the negative tensile force altogether.

Mathematical modelling

Deflection due to uniformly distributed load

The deformations of each cable caused by the allocated load determine the strains in the stiffening girder of a cable-stayed bridge. By studying the deformed geometry of the system, it is possible to calculate the non-linear problem of determining the forces in cables and how they affect the stiffening girder. The first step is to determine how a straightforward beam with elastic supports deforms when the dead weight is evenly distributed.

The authors of this publication are currently engaged in research about the interaction between the cables and stiffening girders of cable-stayed bridges, as obtained analytically (Straupe & Paeglitis 2011. These formulas illustrate the effects of geometric and mechanical characteristics on the system's stresses and deformations. This will enable the use of the Final Element Method (FEM) to make an appropriate initial assumption of these components for subsequent analysis.

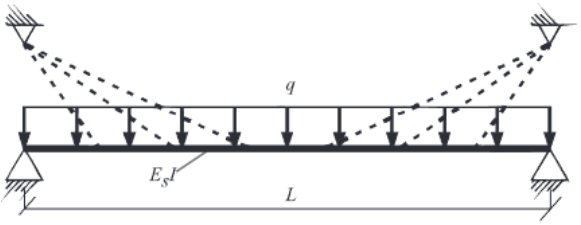

Figure 10: cable-stayed bridge diagram

(1) $y(x) = \frac{q}{24E_sI}(2Lx^3 - x^4 - L^3x)$

Deflection due to the symmetrical applied unit forces

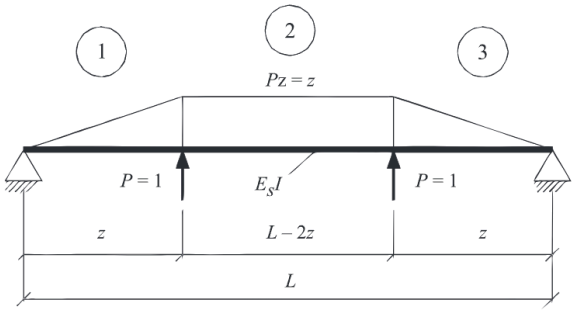

Figure 11: Bending moment diagram due to symmetrical vertical forces.

Using differential equations (see figure 11), the three sections of the corresponding deflection can be found through the three sections with different equations of bending moments as following:

$$(2)\ y_1(x) = \frac{1}{E_s I}\left(\frac{x^3}{6} + \frac{(z^2 - Lz)x}{2}\right)$$

$$(3)\ y_2(x) = \frac{z}{E_s I}\left(\frac{x^2}{2} - \frac{Lx}{2} + \frac{z^2}{6}\right)$$

$$(4)\ y_3(x) = \frac{1}{E_s I}\left(\frac{(x-L)^3}{6} + \frac{(z^2 - Lz)(x-L)}{2}\right)$$

The stiffening girder's bending moment diagram depends on the vertical forces acting on the cable support points. However, the size of these forces is contingent upon the degree to which the cable undergoes deformation (elongation) as a result of the load that is being applied. The cable extension is contingent upon the material's Young's modulus, cross-sectional area, and length (Walther et al. 1999).

$$(5)\ N_0 = \frac{q(2Lz^3 - z^4 - L^3 z)}{\frac{24 E_s I L_v}{E_v F} - 12z^3 + 12Lz^2}$$

$L_V = length\ of\ the\ cable\ (m),\ F = cross\ section\ area\ (m^2)$

$E_v = young's\ modulus\ (kN/m^2)$

$f = elongation\ of\ the\ cable\ (m)\ N_0 = symmetrical\ pair\ of\ vertical\ forces$

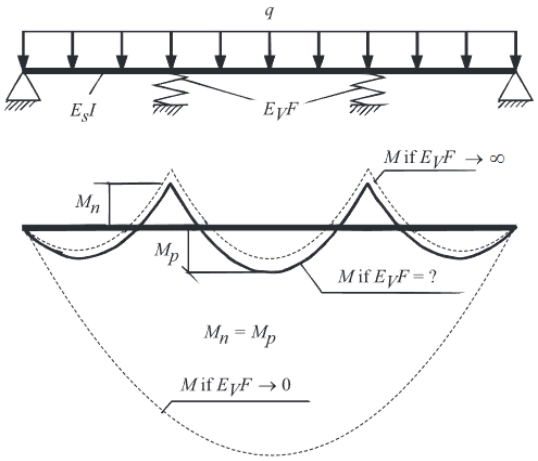

Figure 12 : Bending moment diagram depending on the stiffness support (Walther et al. 1999).

$$(6)\ N_0 = \frac{-M_q(z) - M_q\left(\frac{L}{2}\right)}{M_1(z) + M_1\left(\frac{L}{2}\right)},\ (5)\ into\ (6)\ \to (7)\ E_v F_e = \frac{6E_s IL}{\frac{2Lz^4 - z^5 - L^3 z^2}{z^2 - Lz - \frac{L^2}{3}} + 4z^3 - 3Lz^2}$$

Displacement of anchorage point can be written as:

$$(8)\ f = \frac{N_0 L_v}{E_v F_e} = N_0 L_v \frac{\frac{2Lz^4 - z^5 - L^3 z^2}{z^2 - Lz - \frac{L^2}{4}} + 4z^3 - 3Lz^2}{6E_s IL}$$

, when a cable with real $E_v F$ is chosen , the correlation can be written as :

$$(9)\ f + \Delta = \frac{N_0 L_V}{E_v F}$$

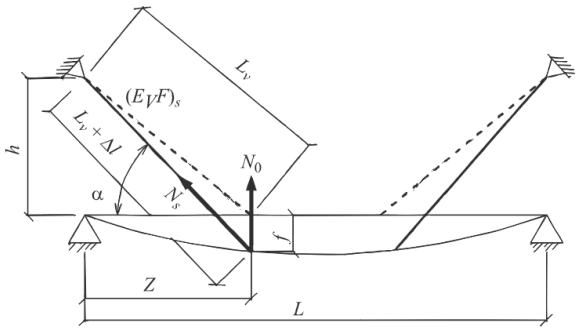

Figure 13: symmetrical deformation of inclined cables (Walther et al. 1999).

The incline of the cable can be considered by determining an appropriate $E_v F_s$ for the cable. This value corresponds to the stiffening girder's deflections that were previously determined. The elongation Δl and the tensile force N_s of an inclined cable can be determined as follows:

$$(10)\ \Delta l = \frac{N_s L_v}{E_v F_s},\qquad (11)\ N_s = \frac{\Delta l E_v F_s}{L_V}$$

$$(12)\ \Delta l = \sqrt{(h + f)^2 + z^2} - L_v$$

$$(13)\ sin\alpha = \frac{h+f}{L_v + \Delta l} = \frac{N_0}{N_s} = \frac{f E_v F L_v}{h \Delta l E_v F_s}$$

$$(14)\ E_v F_s = \frac{f E_v F L_v (L_v + \Delta l)}{h \Delta l (h+f)} = \frac{f E_v F L_v \sqrt{(h+f)^2 + z^2}}{h\left(\sqrt{(h+f)^2 + z^2} - L_v\right)(h+f)}$$

$$where\ L_v = \sqrt{h^2 + z^2}\ (15)\ N_s = \frac{\Delta l E_v F_s}{L_v} = \frac{f E_v F \sqrt{(h+f)^2 + z^2}}{h(h+f)}$$

Symmetrical cables in pair solution

$$(17)\ \begin{cases} y(z_1) + N_1(y_{11}(z_1) - \frac{L_{v1}}{R_v F_1}) + N_2 y_{12}(z_1) + \ldots + N_n y_{1n}(z_1) = 0 \\ y(z_2) + N_1 y_{21}(z_2) + N_2(y_{12}(z_2) - \frac{L_{v2}}{E_v F_2}) + N_3 y_{13}(z_2) + \ldots + N_n y_{1n}(z_2) = 0 \\ \ldots \\ y(z_n) + N_1 y_{21}(z_n) + N_2 y_{22}(z_n) + N_3 y_{23}(z_n) + \ldots + N_n(y_{1n}(z_n) - \frac{L_{vn}}{E_v F_n}) = 0 \end{cases}$$

The maximum and minimum absolute values of the bending movement of the outer section can be determined using the parabolic equation for the graph depicted in the accompanying figure. The optimal span can be determined as the following $b = 0.85L_0 m = 0.85L_0 - 0.5L_0 = 0.35L_0$

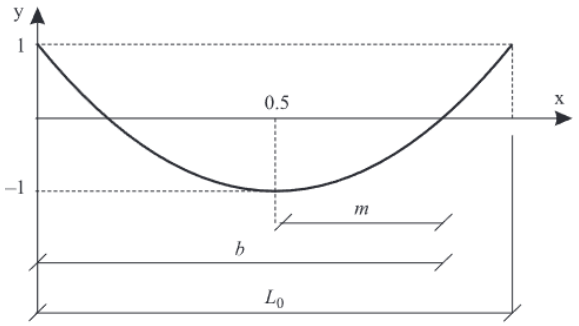

Figure 14: Bending moment diagram of the outer section

Practical Example

The cable-stayed bridge's parameters can be selected and their interaction can be investigated using analytical expressions that have been previously discovered. The FEM program should perform the final calculations to ensure that the data acquired is in accordance with the selected criteria (Bruer et al. 1999). The FEM program has randomly verified the following, and a strong correlation has been identified.

The equations (17) and methodology that have been established should be estimated and their accuracy should be verified using this example. Consequently, certain factors were not taken into account, such as the cable sag effect and the deformations of pylons from the moving masses, which are the subjects of further investigation for this method.

Figure 15 illustrates the cable-stayed bridge system that was analyzed. The pylons are initially adopted by the points of the diagrams provided.

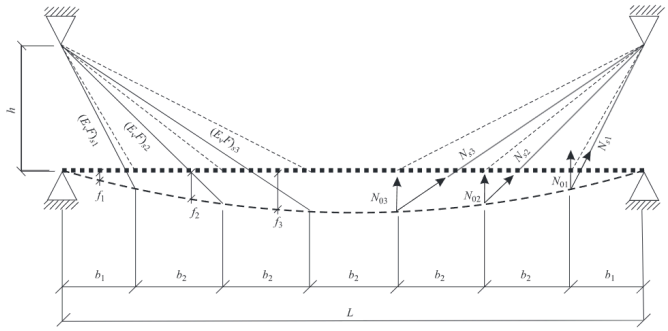

Figure 15 : Deformed shape of the cable-stayed bridge.

height h = 50 meters. The span, which has a length of 231 meters, is divided into seven sections. The paper does not explicitly address the cross-sectional geometry and loads of the structures, as they are not the subject of the paper. At first, the stiffening girder is designed using the following parameters:

- the second moment of area of the stiffening girder: $I = 41.74\, m^4$
- the Young's modulus of the stiffening girder: The stress E_s is equal to 36 GPa, and the normally distributed load $q = 1300\, kN/m$.

In accordance with the assumptions outlined above, the stiffening girder is partitioned into sections:

$b_2 = \frac{L}{2\times 0.85+5} = \frac{231}{6.71} = 34.44\, m,$

$b_1 = 0.85 b_2 = 0.85 \times 34.44 = 29.39\, m$

$M_p = M_n = \frac{M_{load}(\frac{L}{2}) - M_{load}(\frac{L}{2}-\frac{b_2}{2})}{2} = 96.38\, MNm$

Table 1: Bending moments in the specific points

$x\ (m)$	$M_{load}\ (MNm)$	$M_{prestress}\ (MN$	$M_{sum}\ (MNm)$
0.0	0	0	0
12.2	1731.97	− 1635.59	96.38
29.4	3852.27	− 3948.65	− 96.38
46.6	5587.08	− 5490.7	96.38
63.8	6936.36	− 7032.74	− 96.38
81.1	7900.14	− 7803.76	96.38
98.3	8478.4	− 8574.78	− 96.38
115.5	8671.16	− 8574.78	96.38

Table 2: Cable parameters

Cable No	$N_0\ (MN)$	$f\ (mm)$	$N_s (MN)$	$E_V F_s (MN)$
1	44.77	56.67	51.92	61 638
2	44.77	102.62	72.52	92 877
3	44.77	125.59	98.54	19 0618

N_0 *is the tensile force vertical component* ,

f *is the displacement of stiffness of girder* ,

N_s *is the tensile strength is cable* ,$E_v F_s$ *stiffness of the inclined cable*

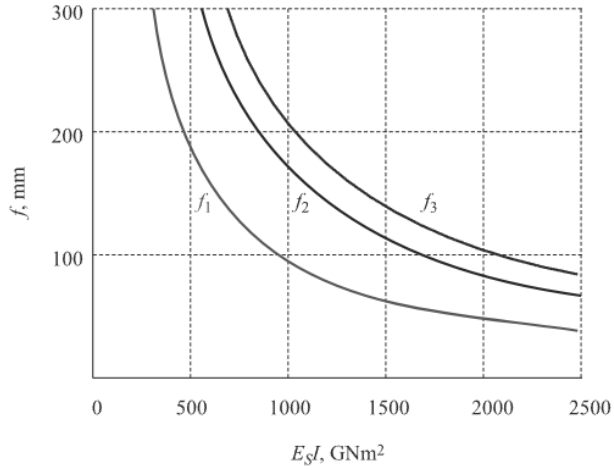

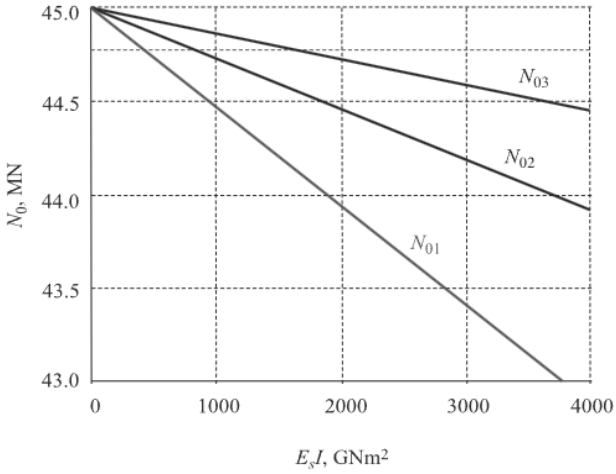

Figure 16: vertical displacement $f(mm)$ of anchorage point of cable and vertical component of $N_0(MN)$depending on the stiffness of the girders (Straupe & Paeglitis 2013).

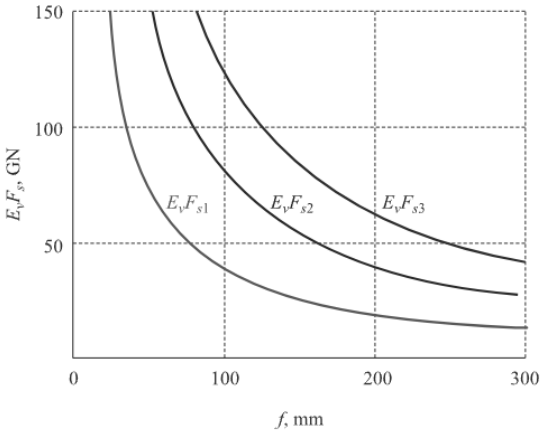

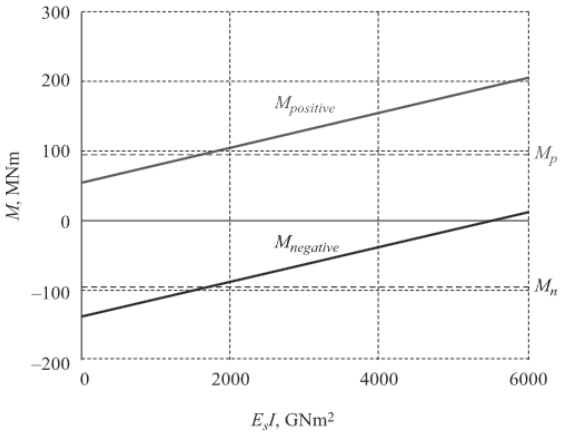

Figure 16 : stiffness of the inclined cables $E_vF_s(GN)$ with respect to displacement $f(mm)$, and Bending moments with respect to stiffness of the stiffening girder (Straupe & Paeglitis 2013).

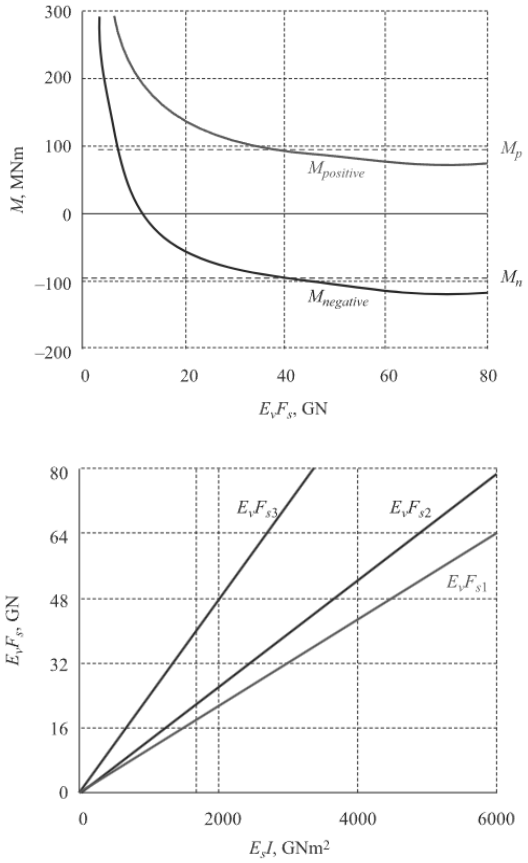

Figure 17: Maximum positive and negative bending moments with respect to the stiffness of cables, and required values of stiffness of cables with respect to girder stiffening (Straupe & Paeglitis 2013).

The analysis of stresses in the stiffening girder concludes that the portion of the span that is situated closer to the pylons is in a more advantageous position due to its higher axial compression force, which reduces or entirely eliminates the tensile stresses caused by the bending moment. A logical objective conducted by (Bruer et al. 1999) is to reduce the bending moments in the midsection of the central span, where the stiffening girder is located, and the axial compression force is lower.

The mathematical model is enhanced to reduce the tensile tensions in the stiffening girder. In areas where it is desirable to reduce the bending moments, it can be accomplished by minimizing the distance between the cable anchor-points. The optimal solution is determined by introducing a parameter dx [m], which denotes the length difference between two adjacent panels.
The bending moments M, axial forces NG, and stresses σ in the upper and lower fibers of the cross-section of the strengthening girders of two systems are compared in Fig. 4. The left panel has a constant length (parameter dx = 0 m), while the right panel has a variable length (dx = 1,0 m). In this instance, temporary supports are employed to achieve erection.

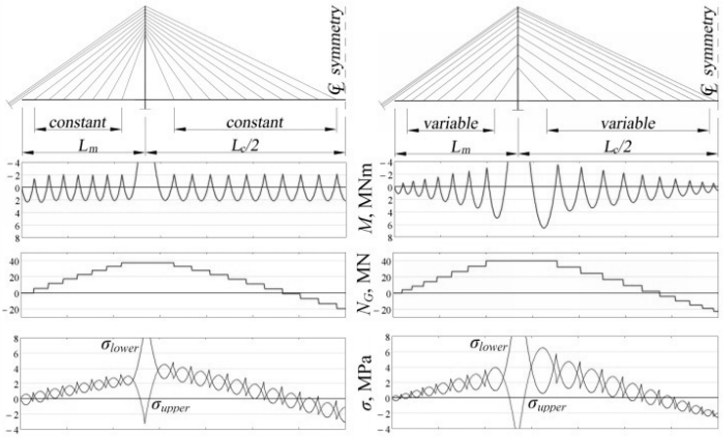

Figure 18: Bending moment diagrams (M), axial force (N_G) and stress (σ) for cable-stayed bridge modification systems(Straupe & Paeglitis 2013).

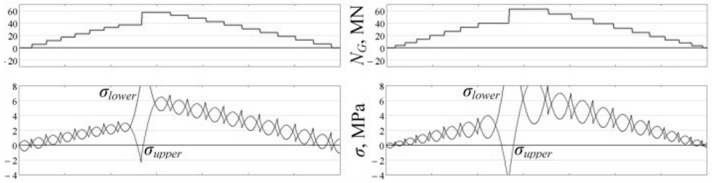

Figure 19: The axial force diagrams in stiffness girder (N_G) and stress (σ) for two modifications of bridge system (Straupe & Paeglitis 2013)

The separation into panels changes the strains developing in a stiffening girder. Improved positioning of cable anchors produced tensile forces and stresses that indicate events on right sides of Figures 4 and 5. Almost completely avoiding tensile stresses is made possible by the best partition of stiffening girder into panels (Straupe & Paeglitis 2013).
The analysis chart in Figure 19 and 20 illustrates the maximum tensile stresses in the central span, which are contingent upon the parameter dx. Stress peaks in the rigid support area at the pylons are not addressed in this section, as they must be prevented through pre-stressing.

Coordination of tensile forces in cables

The tensile forces of the shortest cables (those closest to the pylons) are lower (line No. 1 in both graphs shown in Fig. 7), while the tensile forces of the longer cables are higher (line No. 7 for the back-span and line No. 10 for the central span) when the girder is divided equally into panels (i.e. parameter dx = 0). The tensile forces in Fig. 7 are demonstrated to increase as the parameter dx is increased. The charts demonstrate that the parameter dx has an optimal value, which results in tension forces in all cables at approximately the same levels. In this scenario, the stresses in all cables will be consistent, which is a substantial accomplishment in terms of the durability of the cables.In order to unify forces in all cables, the optimal value of parameter dx is approximately 0.4 m in

the example provided.This value is not best for stiffening girder tensile stress reduction. Therefore, a compromise must be reached.Forces in longer connections tend to decrease while those in shorter cables tend to increase. This consistency is applicable to all cables within the system.

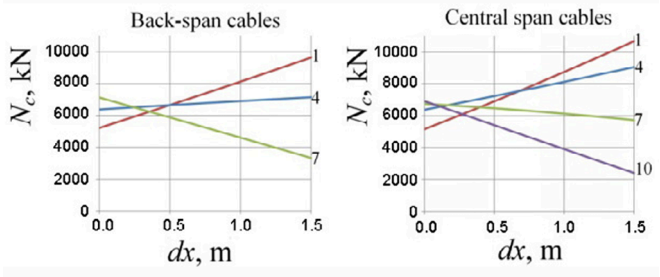

Figure 20: Cable tensile forces based on the distance between anchor points (dx) reduction parameter: Three back-span cables (shortest cable number 1; longest cable number 7)

The effect of variable loads on the anchor heads

Bending moment values must be set for each moving load point. This supposition can be proven by considering that the moment difference between the maximum positive moment (located in the node where the load is located) and the negative moment (located at the end of the panel, in the node where the cable is anchored) for each panel is a constant.

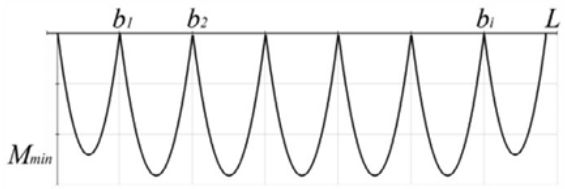

Figure 21: Minimum bending moment in every central section span.

$b_{z1}(z)$ is the coordinate of the point load's starting in the panel, and $b_{z2}(z)$ is the coordinate of the point load's ending in the panel.

The introduction of an "intelligent" cable adjusting system can achieve the bending moment with the least possible extreme values caused by variable loads. This system functions as a group of mechanisms that monitor the displacements of certain nodes and adjust separate cables based on the location and action of the variable loads.

$$(3)\ M_{min}(z) = P_0 \frac{b_{z2}(z)-1}{b_{z2}(z)-b_{z1}(z)}(z - b_{z1}(z))$$

Eq. (3) can be used to determine the constant, which is contingent upon the ordinate z of the point load location. This equation is illustrated graphically in Figure 21

Assume that the optimal bending moment diagram is obtained when the value in the node where the point load is located is $+\ 0.5M_{min}(z)$, but the value at the two extremities of this panel is $+\ 0.5M_{min}(z)$. The vertical component of cable forces N can be determined by solving the system of equations:

$$(4)\ N(z)M_R^{'} + M_P^{'} = \frac{-M_{min}(z)}{2}$$

$M_R =$ *bending moment due to restrain of creep in concrete*

$M_p =$ *Bending moment due to applied weight or force on cable*

$$M_R^{'} = \begin{vmatrix} M_R(b_1,1) & M_R(b_1,2) & \dots & M_R(b_1,i) \\ M_R(b_2,1) & M_R(b_2,2) & \dots & M_R(b_1,i) \\ \dots & \dots & \dots & \dots \\ M_R(b_i,1 & M_R(b_i,2) & \dots & M_R(b_i,i) \end{vmatrix}$$

$$(6)\ M_P^{'}(z) = \begin{vmatrix} M_P(b_1,z) \\ M_P(b_2,z) \\ \dots \\ M_P(b_i,z) \end{vmatrix}$$

As a result of the fact that $M_R(b_j,n) = M_R(b_n,j)$ in matrix (5), the inverse matrix $(M_R)^{-1}$ is created, which only contains members that are not zero around the main diagonal.

$$(7)\ N(z) = (M_R^{'})^{-1}(\frac{-M_{min}(z)}{2} - M_P^{'}(z))$$

$$(8)\ M(x,z) = \sum_{n=1}^{i} N(z)_n M_R(x,n) + M_P(x,z)$$

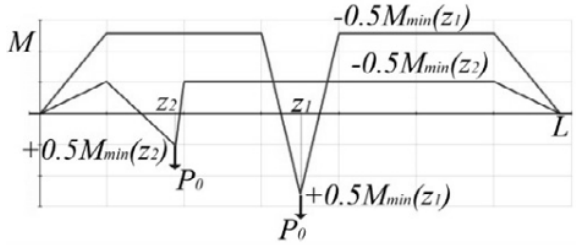

Figure 22: the point load P0 moving across the bridge is applied to nodes z1 = L/2 and z2 = L/4

Modelling pylons and girders

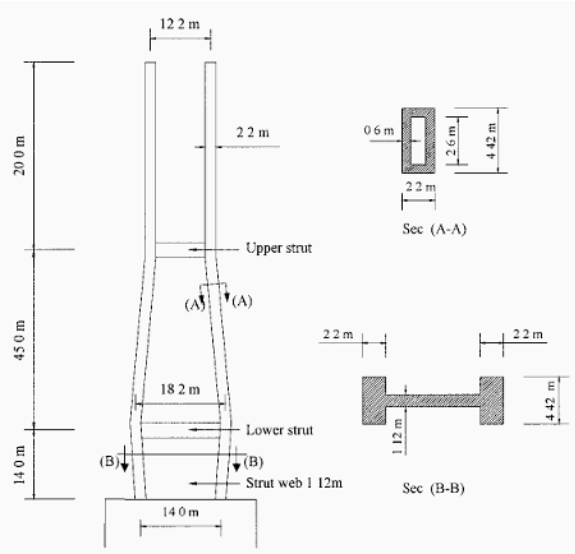

Figure 23: Pylon model dimension (Nazmy & Abdel-Ghaffar 1990)

(1) $[k_T]_b = [k_E]_b + [k_G]_b$

$[k_T]_b = Matrix\ beam\ element,\ tangent\ stiffness$

$[k_E]_b = Elastic\ stiffness\ matrix\ of\ beam$

$[k_G]_b = Geometric\ stiffness\ matrix\ frame$

Cable-stayed bridges, which utilise inclined cable stays to provide elastic support for the deck at various points along its length, are entering a new phase of development. These structures are now being designed for medium to long span lengths, ranging from 400 m to 1500 m for the central span. In Japan, there are proposals to construct even longer cable-stayed bridges, using both prestressed concrete and steel materials. The trend towards longer spans, coupled with the use of more slender or shallow stiffening girders, has raised concerns about the bridges' performance under various dynamic loads, including traffic, wind, and seismic activity.

Given that these long-span, cable-supported structures are complex and exhibit primarily geometric nonlinearity, it is crucial to accurately understand and predict their structural response to these loads. Consequently, there is a significant need in bridge engineering to develop and validate precise methods that can provide a comprehensive understanding of the static, dynamic, seismic, and wind-related issues associated with cable-stayed bridges. This understanding is essential for ensuring the safety and reliability of these increasingly ambitious structures.

Nonlinear analysis three dimensional technique

Three-dimensional long-span cable-stayed bridges are subjected to a set of initial cable tensions and their own dead weight in a nonlinear static analysis. The analysis takes into account all causes of geometric nonlinearity, including cable sag, the interaction of axial force and bending moment in the bridge deck and towers, and changes in the bridge geometry brought on by significant displacements. The study of nonlinear structural systems is somewhat complicated by the fact that their stiffness varies as the structure deforms. In this instance, the stiffness matrix [K] in equation (1) depends on the joint displacements {D}, which are not yet known. The set of nonlinear stiffness equations requires a computational program to solve. Consequently, such nonlinear equations for the displacement vector {D} are typically solved numerically(Pao & Chen 2009).

The following assumptions and approximations were made to facilitate the nonlinear static analysis:
(1) The elastic limit is maintained for all stresses in the bridge's constituent parts.
(2) At their connection places, all cables are fastened to the bridge and the tower.
(3) The cable stays between the towers and the bridge girder are all of the same section and are thought to be straight chord links. These links are given an equivalent axial stiffness to offset the sag effect.
(4) It is assumed that cables are completely flexible, meaning that their flexural stiffness can be ignored.

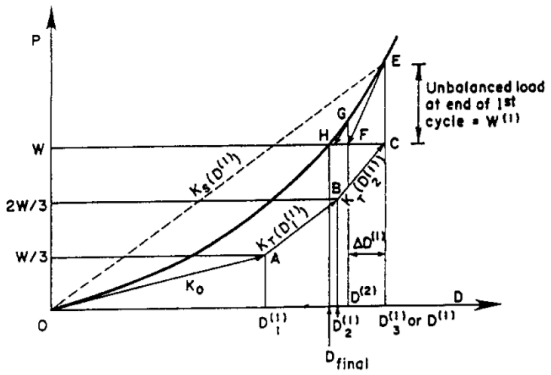

Figure 24: Mixed procedure used for the nonlinear static Analysis (Nazmy & Abdel-Ghaffar 1990).

The joint displacements $\{D_1^{(1)}\}$ are then calculated using equation (1) with $\{P\} = \frac{1}{3}\{W\}$ after the initial load increment is applied using the tangent stiffness matrix of the undeformed structure $[K_0]$. The incremental joint displacements brought on by the second load increment are then calculated using the tangent stiffness matrix $K_T(D_1^{(1)})$ that corresponds to the structure's displaced shape. To produce $\{D_2^{(1)}\}$, these incremental displacements are then added to the joint displacements that were previously calculated$\{D_2^{(1)}\}$. This corresponds to point B in the figure. The process is repeated for the final load increment till reaching point C, which marks the end of the first cycle. The computed displacements at the conclusion of the cycle $\{D_1^{(1)}\}$ (or simply $\{D^{(1)}\}$, correspond to loads on the genuine load

displacement curve, specifically point E. Line CE represents the unbalanced loads at the end of the first cycle, $\{W^{(1)}\}$. These loads are then applied as a new set of joint loads during the second cycle of iteration, using the tangent stiffness $K_T(D^{(1)})$ represented by line EF.

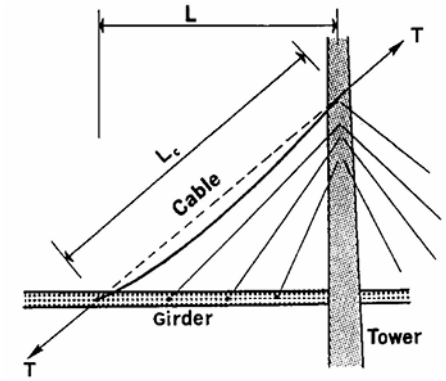

Figure 24.1: incremental measurements to be used in calculation

The incremental displacements are calculated from:

(1) $[K]\{D\} = \{P\}$

(2) $[K_T(D^{(i)})]\{\Delta D^{(i)}\} = \{W^{(i)}\}$

(3) $\{W^{(i)}\} = \{W\} - [K_s(D^{(i)})]\{D^{(i)}\}$

$[K] = global\ stiffness\ matrix\ of\ the\ structure,$

$\{D\} = vector\ joint\ displacement,$

$\{P\} = vector\ of\ applied\ joint\ load$

$\{W^{(i)}\} = out\ of\ balance\ force\ vector\ computed\ from$

$[K_s(D^{(i+1)}] = secant\ stiffness\ matrix\ of\ the\ structure$

$when\ joint\ displacement\ are\ \{D^{(i)}\}$

(4) $\{D^{(i+1)}\} = \{D^{(i)}\} + \{\Delta D^{(i)}\}$

(5) $[k] = [r_m]^T[k_m][r_m]$

$[k_m] = member\ stiffness\ matrix\ in\ global\ coordinates$

$[r_m] = rotation\ matrix$

(6) $[r_m] =$

$$\begin{bmatrix} [r] & 0 & 0 & 0 \\ 0 & [r] & 0 & 0 \\ 0 & 0 & [r] & 0 \\ 0 & 0 & 0 & [r] \end{bmatrix}$$

(7) $E_{eq} = \dfrac{E}{1+[\frac{(wL)^2AE}{12T^3}]}$ (Ernst 1965)

$E_{eq} = equivalent\ modulus E = cable\ material\ effective\ modulus$

$L = horizontal\ projected\ length\ of\ the\ cable\ ,$

$w = weight\ per\ unit\ length\ of\ the\ cable$

$A = cross - sectional\ area\ of\ the\ cable$

$T = cable\ tension$

(8) $E_{eq} = \dfrac{E}{1+[\frac{(wL)^2(T_i+T_f)AE}{12T_i^2T_f^2}]}$

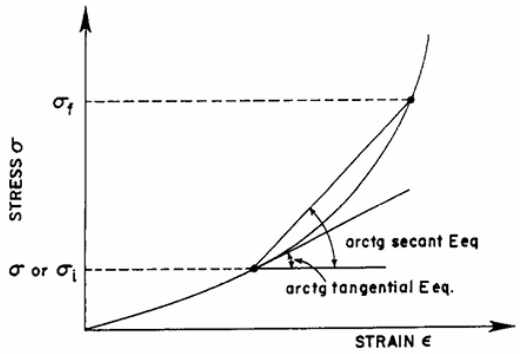

Figure 25: Non-linear stress strain curve (Nazmy & Abdel-Ghaffar 1990).

(9) $\left|k_E\right|_c = \dfrac{AE_{eq}}{L_c}$

$$\begin{bmatrix} 1 & -1 \\ -1 & 1 \end{bmatrix}$$

(10) $[k_T]_c = [k_E]_c + [k_G]_c$

$[k_T]_c = the\ element\ tangent\ stiffness\ matrix\ in\ local\ coordinate$

$[k_E]_c = elastic\ matrix\ stiffness\ in$ (9)

(11) $\left|k_G\right|_c = \dfrac{AE_{eq}}{L_c}$

$$\begin{bmatrix} [G]_c & -[G]_c \\ -[G]_c & [G]_c \end{bmatrix} \quad 6 \times 6$$

(12) $Submatrix\ [G]_c =$

$$\begin{bmatrix} 0 & 0 & 0 \\ 0 & 1 & 0 \\ 0 & 0 & 1 \end{bmatrix}$$

Formulation of nonlinear stiffness for cable components

As previously mentioned, the tower and girder elements of a cable-stayed bridge undergo significant deformations as a result of the combined effects of high axial forces and large bending moments. This results in a strong coupling between the axial and flexural stiffness of the members. This coupling can be accounted for in the refined non-linear analysis by incorporating the concept of stability function (Nazmy & Abdel-Ghaffar 1990)

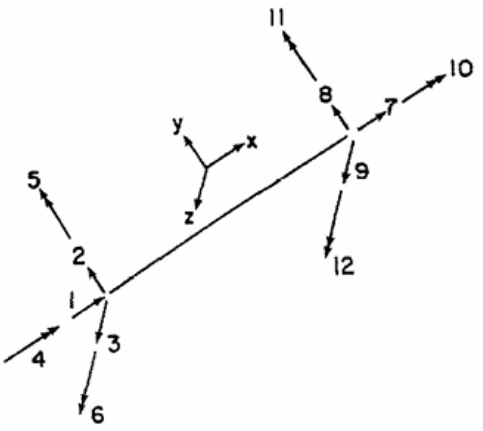

Figure 26: degree of freedom of a beam element in local coordinates

$$(13)\ [k_E]_b = \begin{bmatrix} k(1,1) & k(1,2) & .... & .... & k(1,12) \\ k(2,1) & k(2,2) & .... & .... & k(2,12) \\ .... & .... & .... & .... & .... \\ .... & .... & .... & .... & .... \\ k(12,1) & k(12,2) & .... & .... & k(12,12) \end{bmatrix}$$

where Z is the cross-section torsional moment of inertia, G is the member material shear modulus, S's are the stability functions, and E is the member material modulus of elasticity. A, L, and Z are the cross-sectional area, lenghth , and cross-sectional moments of inertia about the local principal y and z axes, respectively. The bending stiffness of the member is modified about the local y axis by S1 through S4, while the bending stiffness is modified about the local z axis by S1 through S4, and the axial rigidity is modified by S5. The value of one is assigned to all of these S's if the axial force in the bending member is zero. The axial force P and the member end moments Ml and M2 at both ends about the local y and z axes of the member can be used to express the stability functions, as defined in Fig. 10.

$(14)(a)\ k(1,1) = k(7,7) = -k(1,7) = -k(7,1) = (EA/L)S5$

$(14)(b)\ k(2,2) = k(8,8) = -k(2,8) = -k(8,2) = (12EI_z/L^3)SI_z$

$(14)(c)\ k(3,3) = k(9,9) = -k(3,9) = -k(9,3) = 12(EI_y/L^3)SI_y$

$(14)(d)\ k(2,6) = k(6,2) = k(2,12) = k(12,2) = -k(6,8)$
$= -k(8,12) = -k(12,8) = (6EI_z/L^2)S2_z$

$(14)(e)\ k(3,5) = k(5,3) = k(3,11) = k(11,3)$
$= -k(5,9) = -k(9,5) = -k(9,11) = -k(11,9) = (-6EI_y/L^2)S2_y$

$(14)(f)\ k(4,4) = k(10,10) = -k(4,10) = -k(10,4) = GI_x/L$

$(14)(g)\ k(5,5) = k(11,11) = (4EI_y/L)S3_y$

$(14)(h)\ k(6,6) = k(12,12) = (4EI_z/L)S4_y$

$(14)(i)\ k(5,11) = k(11,5) = (2EI_y/L)S4_y$

$(14)(j)\ K(6,12) = k(12,6) = (2EI_z/L)S4_z$

For tensioning a member (P is positive), the stability function $S1_z$ through $S4_z$ are

$(15)(a)\ SI_z = \omega^3 sinh\omega/12R_l$, $(15)(b)\ S2_z = \omega^3 cosh\omega - 1/6R_l$,

$(15)(c)\ S3_z = \omega(\omega cosh\omega - sinh\omega)/4R_l$,

$(15)(d)\ S4_z = \omega(sinh\omega - \omega)/2R_l$,

$(15)(c)\ S3_z = \omega(\omega cosh\omega - sinh\omega)/4R_t$,

$(15)(d)\ S4_z = \omega(sinh\omega - \omega)/2R_l$,

$since\ (16)\ \omega = \mu L\ and\ \mu^2 = P/EI_z$

$and\ (17)\ R_l = 2 - 2cosh\omega + \omega sinh\omega$, when compression member P is negative. $(18)(a)\ SI_z = \omega^3 sinh\omega/12R_c$,

$(18)(b)\ S2_z = \omega^2(1 - cosh\omega)/6R_c$, $(18)(c)\ S3_z = \omega(sin\omega - \omega cos\omega)4R_c$

,$(18)(d) S4_z = \omega(\omega - sin\omega)/2R_c$, $with\ (19)\ R_c = 2 - 2cos\omega - \omega sin\omega$

In the same manner, by substituting I_z by I_y for in equations (15) through (20), the stability functions SI_y through $S4_y$ can be found. When P is positive for a tension member, The following is how to obtain the stability function $(20)\omega = \mu L\ and\ \mu^2 = P/EI_z$,

$(21)\ S5 = 1/[1 - EA(R_{tmy} + R_{tmz})/4P^3L^2]$,

$where\ (22)\ R_{tmy} = \omega_y(MI_y^2 + M2_y^2)(coth\omega_y + \omega cosech^2\omega_y)$
$- 2(m1_Y + M2_y)^2 + (M1_yM2_y)$
$\times (1 + \omega_y coth\omega_y)(2\omega_y cosech\omega_y)$, $(23)\ \omega_y = \mu_y L\ and\ \mu_y^2 = P/EI_y$,

$and(24)\ R_{tmz} = \omega_z(M1_z^2 + M2_z^2)(cot\omega_z + \omega_z cosec^2\omega_z)$
$- 2(M1_z + M2_z)^2 + (M1_zM2_z) \times (1 + \omega_z cot\omega_z cosec\omega_z)$

$(25)\ \omega_z = \mu_y L\ and\ \mu_y^2 = P/EI_z$

when compression for member P is negative

$(26)\ S5 = 1/[1 - EA(R_{cmy} + R_{cmz})/4P^3L^2]$,and

$(27)\ R_{cmy} = \omega_y(M1_y^2 + M2_y^2)(cot\omega_y + \omega_y cosec^2\omega_y) - 2(M1_y + M2_y)^2$
$+ (M1_zM2_z) \times (1 + \omega_z cot\omega_z cosec\omega_z)(2\omega_y cosec\omega_y)$

$(28)\ \omega_y = \mu_y L\ and\ \mu_y^2 = P/EI_y$

$(29)\ R_{cmz} = \omega_y(M1_z^2 + M2_z^2)(cot\omega_z + \omega_z cosec^2\omega_z) - 2(M1_y + M2_y)^2$
$+ (M1_zM2_z) \times (1 + \omega_z cot\omega_z cosec\omega_z)(2\omega_y cosec\omega_y)$

$(30)\ \omega_z = \mu_z L\ and\ \mu_z^2 = P/EI_z$ $(31)[K_T]_b = [K_E]_b + [K_G]_b$

The secant stiffness matrix is actually the stiffness matrix of a beam-column element as provided by equation (13)

Nonlinear strain-displacement relationships and the big deflection theory can be used to determine the tangent stiffness matrix of such an element where P is the axial force and L is the length.

$$(32)\ [K_G]_b = \frac{P}{L}$$

$$\begin{bmatrix}
0 & & & & & & & & & & \\
0 & \frac{6}{5} & & & & & & & & & \\
0 & 0 & \frac{6}{5} & & & & & & & & \\
0 & 0 & 0 & 0 & & & & & & & \\
0 & 0 & -\frac{L}{10} & 0 & \frac{2}{15}L^2 & Symm & & & & & \\
0 & \frac{L}{10} & 0 & 0 & 0 & \frac{2}{15}L^2 & & & & & \\
0 & 0 & 0 & 0 & 0 & 0 & 0 & & & & \\
0 & -\frac{6}{5} & 0 & 0 & 0 & -\frac{L}{10} & 0 & \frac{6}{5} & & & \\
0 & 0 & 0 & 0 & \frac{L}{10} & 0 & 0 & 0 & \frac{6}{5} & & \\
0 & 0 & 0 & 0 & 0 & 0 & 0 & 0 & 0 & 0 & \\
0 & 0 & -\frac{L}{10} & 0 & -\frac{L^2}{30} & 0 & 0 & 0 & \frac{L}{10} & 0 & \frac{2}{15}L^2 \\
0 & \frac{L}{10} & 0 & 0 & 0 & -\frac{L^2}{30} & 0 & -\frac{L}{10} & 0 & 0 & 0 & \frac{2}{15}L^2
\end{bmatrix}$$

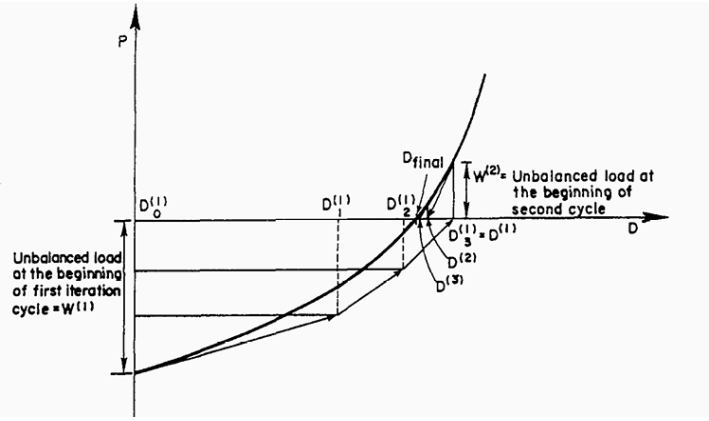

Figure 27 : non linear analysis technique used in algorithms (Nazmy and Abdel-Ghaffar 1990).

Unit force of linear equation set up

Following the definition of the "ideal" dead load force diagrams, the system of unit forces can be mathematically equivalent to these diagrams.

Then the process of finding out the tensioning order and amount, the building order for the deck and pylons, and any needed effects for pre-fabricating the deck and pylons starts.

Principle of Process:

- To determine appropriate member sizes, the unit loading system is first established for the final stage structure. In order to demonstrate structural integrity, this procedure typically entails redefining some member sizes and running the program again.
- The "unit force method" can be applied to the study of the building stage when suitable values have been obtained.
- Every stage of construction may be examined and shown to comply with the design.

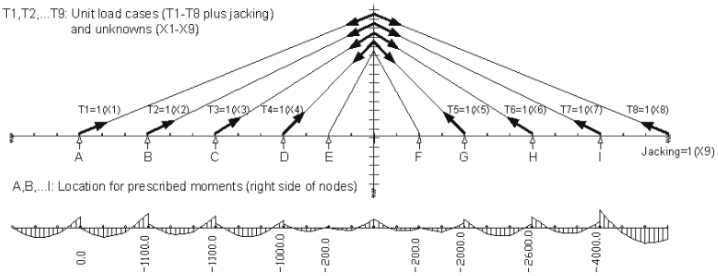

Figure 28: Bending Moment and stress distribution based on applied tension cable reaction load (Bruer et al. 1999).

(1) $M_A = M_P + (M_{T1=1} . X_1) + (M_{T2=1} . X_2) + ... (M_{T8=1} . X_8) + (M_{TJ} . X_9)$

(2) $M_I = M_P + (M_{T1=1} . X_1) + (M_{T2=1} . X_2) + ... (M_{T8=1} . X_8) + (M_{TJ} . X_9)$

M_A ... M_I is the final stage moment at the current position (inc. tensioning and jacking)

M_P Permanent load moment at the current position (without tensioning or jacking)

$M_{T1=1}$... $M_{T8=1}$ bending moment brought on by the tensioning of each unit in its current location.

M_J Bending moment brought on by the end support's unit jacking in its current location

Pylon anchorage design

It is common for stress-disturbed regions (D-regions) to have irregular shapes in a cable-stayed bridge. This makes the cable-pylon anchorage zone an important part that is hard to build. Nevertheless, the pylon anchorage zone lacks specific guidelines in the existing standards and codes, necessitating a trial-and-error approach to its design. This approach involves costly full-scale model experiments and intricate FEM analyses (Wu et al. 2017). The current approach is inefficient, uncertain, and heavily reliant on the designers' experience. Consequently, it is imperative to acknowledge the mechanical behavior of the cable-pylon anchorage zone and streamline the design.

Configuration of the strut and tie (STM) model

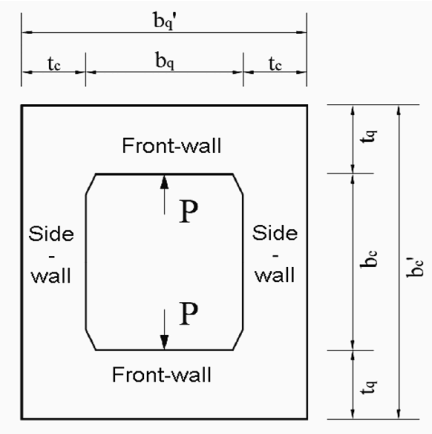

Figure 29: cross section of a pylon wall thickness

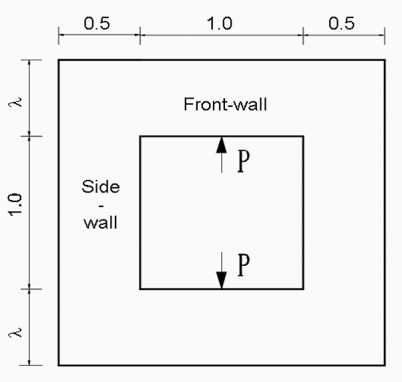

Figure 30: Pylon dimensions in anchorage zone

on the basis of specific criteria, introduces finite-element modifications into the optimization process. Stiffness, weight, frequency, or von Mises stress are some of the other possible criteria. The specification for the maximum stiffness topology design is typically a uniform strain energy density. This means that the optimal structure will be achieved by progressively eliminating the elements with lower strain energy densities from the initial design domain. (Liang & Steven 2002) proposed the performance index (PI) as a metric for evaluating the efficacy of the topology. The front-wall is the primary focus of this paper, and the ratio between the thickness and width of the front-wall is denoted as $\lambda = t_q/b_q$.

(1) $PI = \frac{C_0 V_0}{C_i V_i}$ where $PI = performance\ index$, $C_0 = mean\ compliance$, $V_0 = actual\ volume$, C_i, $V_i = ith\ iteration$

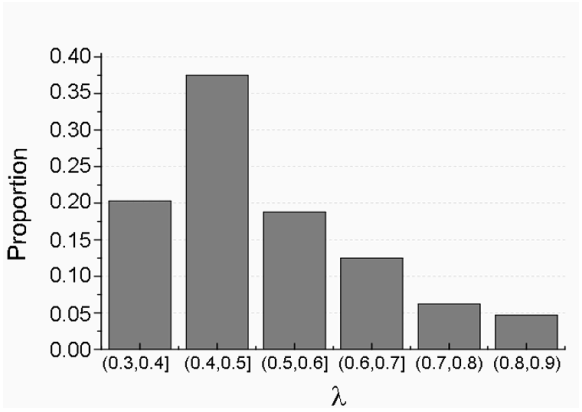

Figure 31: λ distribution for horizontal plane model cable-pylon

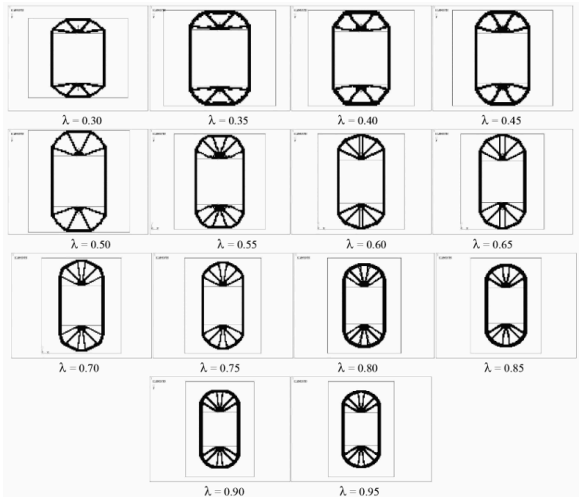

Figure 32: Demonstration of cable pylon anchorage zone topology (Cui & Huang 2019).

Two categories are discerned in the initial configuration: When $\lambda < 0.6$, the symmetric line of the front-wall does not produce a vertical bar; when $\lambda \geq 0.6$, one vertical bar (or two bars with a small angle between them) is generated. The height of the arch formed by the bars in the front-wall will cease to fluctuate once it reaches a specific value, and the apex of the arch will separate from the outer margin of the front-wall. The arch is unable to completely develop when it is small and constrained by the thickness of the front wall, and the top of the arch degenerates into a horizontal bar. The anchorage zone can be categorized into two categories based on the presence of a vertical bar on the symmetric line of the front wall: thin anchorage zone $\lambda < 0.6$ and dense anchorage zone $\lambda \geq 0.6$.

The anchorage zone's initial design domains, which will differ depending on the value of λ, are illustrated in Figure above. The width is set to 1 and the thickness is set to 0.5, with the side-wall dimension being disregarded. The four-node square plane element, which has a length of 1/40, is employed. Two parameters that are associated with evolutionary structural optimization (ESO) are the rejection rate (RR) and the evolution rate (ER), both of

which are equal to 0.01. When the maximal PI is achieved, the optimal topology is achieved, as illustrated in Figure above. The results of the experiment with varied values are presented.

Using a network of "struts" (compressive members) and "ties" (tension members) to illustrate the intricate stress distribution within the concrete structure, this simplified structural analysis model represents the forces acting on the anchorage zone of a cable-stayed bridge pylon, where the stay cables connect to the concrete tower. In essence, it simplifies the complex geometry by dividing it into a network of triangular elements for simpler load path and stress calculations.

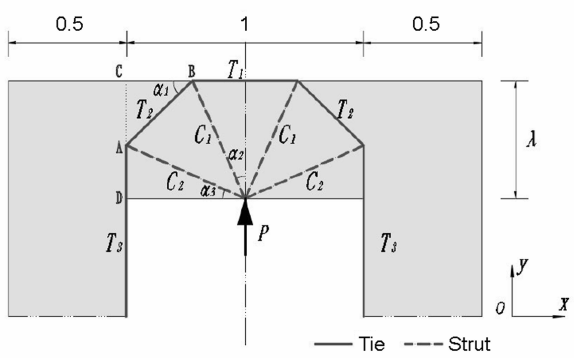

Figure 33: Strut and tie model (STM) in a thin anchorage zone (Cui & Huang 2019).

(3) $U = \frac{1}{2}\Sigma F_i l_i \varepsilon_i \Rightarrow min,$ In the entire STM, the reinforcing steel ties are the primary source of strain energy due to the significantly higher stiffness of the concrete struts. Eqn (2) can be converted into the following when the reinforcement number of ties is determined using the yield strength of reinforcement: (4) $U_T = \frac{1}{2}\Sigma F_i l_i \varepsilon_y \Rightarrow min,$ (5) $l_{AC} = l_{BC} = \frac{1}{2} - \frac{l_{T1}}{2} = \frac{1}{2} - \lambda tan\alpha_2$, (6) $l_{AD} = \lambda - l_{AC} = \lambda - \frac{1}{2} + \lambda tan\alpha_2$,

(7) $l_{T2} = csc\alpha_1 . l_{AC} = \frac{\sqrt{2}}{2} - \sqrt{2\lambda} tan\alpha_2$,

(8) $l_{C_2} = \sqrt{{l_{AD}}^2 + (\frac{1}{2})^2} = \sqrt{\left(\lambda - \frac{1}{2} + \lambda tan\alpha_2\right)^2 + (\frac{1}{2})^2}$,

(9) $tan\alpha_3 = 2l_{AD} = 2\lambda - 1 + 2\lambda tan\alpha_2$,

(10) $l_{T3} = b_c + l_{AD} = \frac{b_c}{2} + \lambda - \frac{1}{2} + \lambda tan\alpha_2$, equilibrium in y direction; (11) $F_{T_3} = \frac{P}{2}$, (12) $F_{T1} = \frac{P}{4\lambda}$(13) $F_{C_2} . cos\alpha_3 - F_{T2} . cos\alpha_1 = 0$, for isolating point A, $\Sigma F_X = 0$ (13) $F_{C2} . cos\alpha_3 - F_{T2} . cos\alpha_1 = 0$,

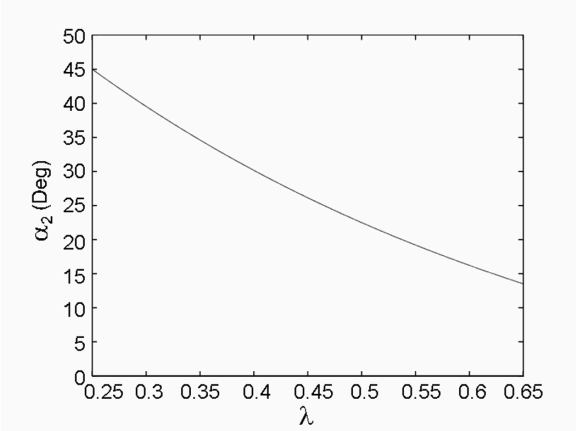

Figure 34 : λ , α_2 relationship for thin anchorage zones (Cui & Huang 2019).

since $\Sigma F_y = 0$: (14) $F_{T_3} = F_{C2} . sin\alpha_3 + F_{T2} . sin\alpha_1$, substituting equations (13), (14), (8) and (10) we obtain (15) $F_{T2} = \frac{P}{2\sqrt{2\lambda}(1+tan\alpha_2)}$, (16) $U_T = \frac{1}{2}\varepsilon_y \Sigma F_{Ti} l_{ti} = \frac{1}{2}\varepsilon_y P\left[\frac{1-2\lambda tan\alpha_2}{\lambda(1+tan\alpha_2)} + tan\alpha_2 + b_c + 2\lambda - 1 + 2\lambda tan\alpha_2\right]$, (17) $\frac{\partial U_T}{\partial \alpha_2} = 0$, (18) $\frac{-sec^2\alpha_2(2\lambda+1)}{\lambda(1+tan\alpha_2)^2} + sec^2\alpha_2 + 2\lambda sec^2\alpha_2 = 0$,

(19) $\alpha_2 = 1.36\lambda^2 - 2.58\lambda + 1.34$

Table 2: bar forces in a thin anchorage zone

λ	P	F_{T1}	F_{T2}	F_{T3}
0.3	1	0.83	0.65	0.5
0.35	1	0.71	0.6	0.5
0.4	1	0.63	0.56	0.5
0.45	1	0.56	0.53	0.5
0.5	1	0.5	0.5	0.5
0.55	1	0.45	0.48	0.5

Thick anchorage zone for $\lambda \geq 0.6$

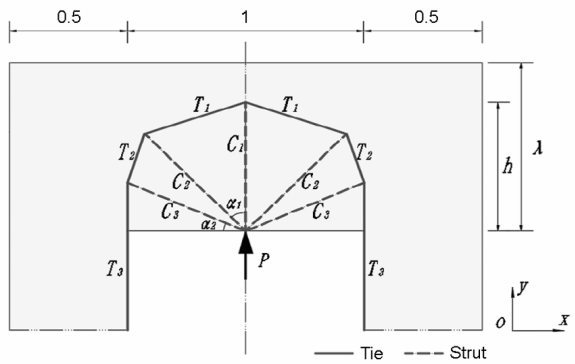

Figure 35: Strut and tie model (STM) in a thick anchorage zone.

Vectorizing the thick anchorage zone's ideal topology in the previous figure yields the model of definitely, indicating that the primary geometric parameters won't alter with λ, only if $0.6 \leq \lambda < 0.65$, the model is uniformly scaled then $l_{c1} = l_{c2}$, $\alpha_1 = 41^{\circ}$, and $\alpha_2 = 26^{\circ}$, when $0.6 \leq \lambda < 0.65$,$h = \lambda$, when $\lambda \geq 0.65$, $h = 0.65$.

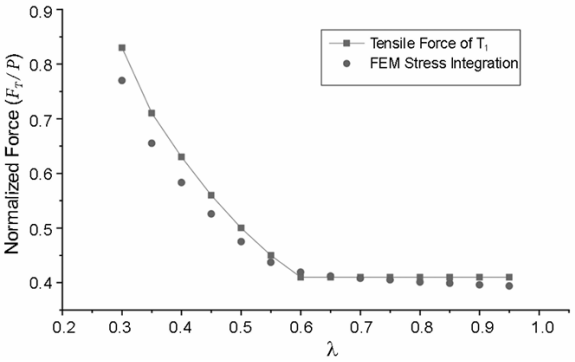

Figure 36: Normalised force distribution with respect to anchorage zone depth(Cui & Huang 2019).

(20) $A_p \geq \frac{T_s}{\phi \sigma_{pe}}$, *where* A_p = *area of prestress tendons*, T_S = *tension force of strut*, $\phi = 0.75$ *strength reduction factor*, *where* σ_{pe} = *effective prestress*

$\sigma_{pe} = 0.6\sigma_{con}$ *for curved prestress*,

$\sigma_{pe} = 0.74\sigma_{con}$ *when prestress tendons are straight*

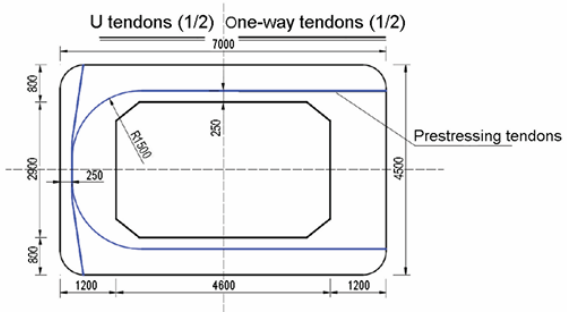

Figure 37: prestressed concrete tendons for pylon design for thin anchorage zone.

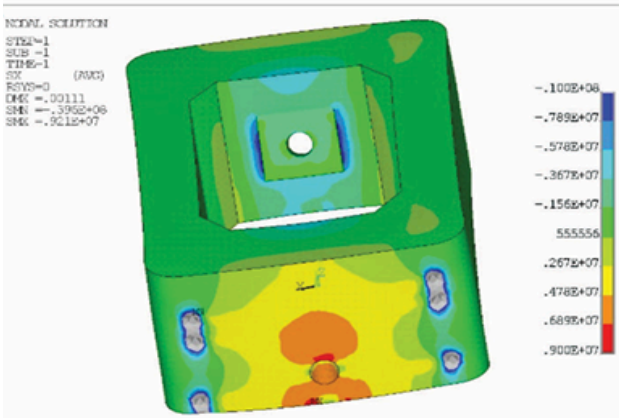

Figure 38: Stress design distribution of cable pylon with one way tendons (Cui & Huang 2019).

Mechanism of shear failure in deep columns of reinforced concrete

This study created a cracking strut-and-tie model (CSTM) to analyze the shear failure of RC deep beams, with a focus on the impact of diagonal cracks on the strut (refer to Figure). These assumptions are made for simplicity in the proposed CSTM:

(1) The interface BC between the diagonal strut and the CCC node is reached by all flexural and flexural-shear fractures. Consequently, the flexural-shear fractures diagonally traverse a portion of the strut. The critical shear of the fractures is the diagonal crack that is closest to the support plate. Consequently, the maximal crack width and tensile strain of the reinforcing bars are observed at the beam bottom, and they decrease linearly to zero at the BC interface.

(3) The compressive failure of the strut at the interface BC governs the shear failure of deep beams. The interface BC is divided into interfaces BM and MC by the CSC. Shear tests reveal two frequent failure types for deep beams: (1) shear-compression failure (discussed in Section 2) and (2) pure compression failure of the entire strut. A shear-compression failure occurs in the CSTM when the effective compressive strength of the interface MC below the CSC is less than that of the interface BM above the CSC.

Conversely, the pure compression failure occurs when the effective strength of the interface BM is equivalent to that of the interface MC.

The strut is divided into two sections by a crack (CSC).

(2) The crack width and reinforcement strain are distributed linearly along

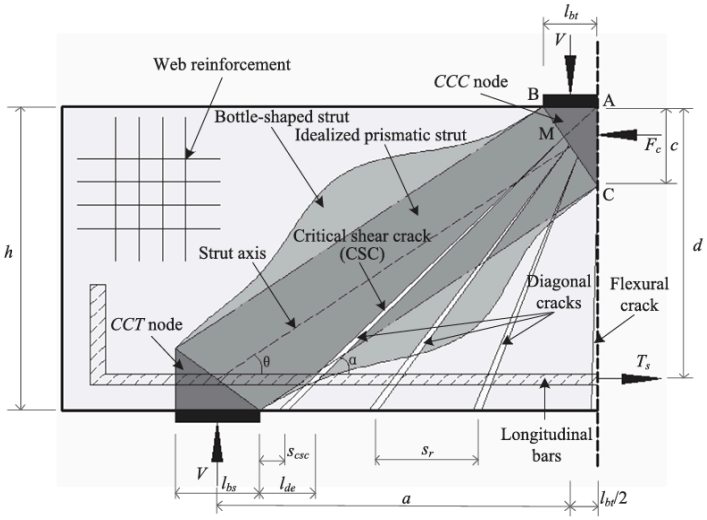

Figure 39: strut and tie crack model of a thick anchorage zone(Chen et al. 2018).

The line MN shown in figure 40 is parallel to the axis of the strut, and point M is defined as the intersection of the CSC and interface BC. The effective compressive strength of the strut in relation to the interface BM is equivalent to the ultimate compressive strength of a standard concrete strut, as the resultant force Fsi on the interface BM is transferred to the region of the strut that is not affected by the diagonal cracks. It is important to acknowledge that splitting fractures parallel to the strut axis may develop in the region above the critical shear strength (CSC) (Birrcher et al. 2009). However, the ultimate strength of the strut is not significantly impacted by the splitting cracks (Laughery & Pujol 2015). This analysis therefore disregards the splitting cracks. On the other hand, the effective compressive strength degradation brought on by the diagonal cracks should be considered since the force Fsc that results on the interface MC is transferred to the cracked area of the strut. Consequently, the strut efficiency coefficients should be applied to the two strut interfaces independently. The aggregate interlock action is activated by the slip between the CSC surfaces, which is a result of the varying stress states of the two portions of the strut.

(1) $F_{si} = \sigma_{ci} w_{si} b = k_c \beta_{si} f_c^{'} w_{si} b$

(2) $F_{sc} = \sigma_{cc} w_{sc} b = \beta_{sc} f_c^{'} w_{sc} b$

F_{si} and F_{sc} ultimate resultant forces on the BM and MC interfaces and $\sigma_{ci} = effective\ compressive\ strength\ of\ the\ uncracked\ part$, where $k_c = (1 - f_c^{'}/250)$ (Almelda 2000) since $f_c^{'} is\ the\ cylinder\ compressive\ strength\ of\ concrete$

$\beta_{si}\ and\ \beta_{sc}\ are\ the\ coefficients\ related\ to\ the\ strut\ efficiency\ in\ different\ interfa$

(3) $V_n = (F_{si} + F_{sc}).sin\theta, V_n = total\ shear\ strength$

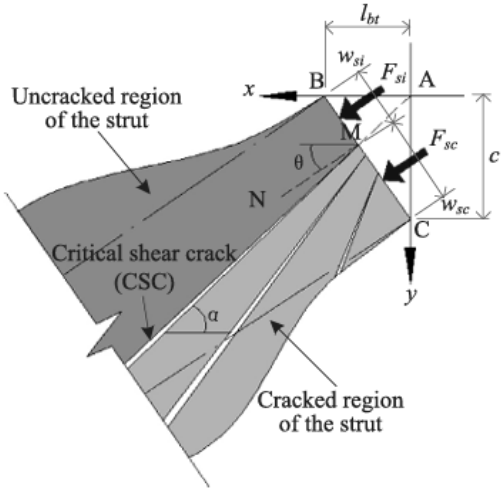

Figure 40: strut with diagonal cracks near CCC nodes (Chen et al. 2018).

Assuming that the point A is the origin of the coordinate, the critical shear crack form and incline stress with the interface BC with an angle α parallel with the longitudinal bar.

(4) $w_{si} = \left[tan\theta.\, l_{bt} + \frac{c.(tan\alpha - tan\theta)}{tan\alpha + c/l_{bt}}\right] cos\theta$

$w_{sl}\ and\ w_{sc}\ = strut\ widths,\ perpendicular\ to\ MN$

$for\ BM\ and\ MC\ respectively$

(5) $w_{sc} = \left[c - \frac{c.(tan\alpha - tan\theta)}{tan\alpha + c/l_{bt}}\right] cos\theta,$

(6) $tan\theta = \frac{d - c/2}{a}$ (7) $tan\alpha = \frac{h}{\alpha + l_{bt}/2 - l_{bs}/2 - s_{csc}}$

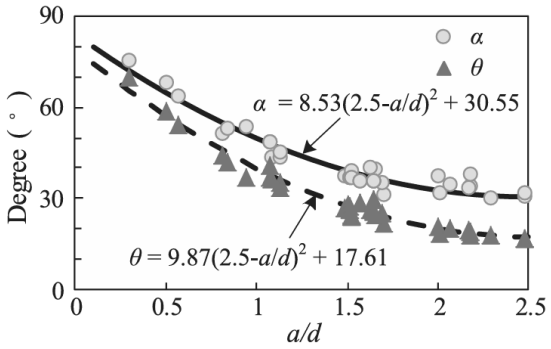

Figure 41 : Variance of CSC angle α and strut angle θ according to the shear span depth ratio (Jin-Keun & Yon-Dong 1994).

(8) $\alpha = 8.53(a/d - 2.5)^2 + 30.55 \geq arctan\left(\frac{h}{a + (l_{bt}/2) - (l_{bs}/2)}\right)$

Solving the following equation (9) the compression zone depth c can be obtained.

(9) $c^2 + 2n\left[\rho d + \rho'(h = d') + \frac{4}{3}\rho' d'(h - d') + \rho d^2 + \frac{2}{3}\rho_h d^2\right] = 0$

where, $n = \frac{E_S}{E_c}$,

ρ *and* ρ' *ratios of longitudinal tension and compression bars*

$d' = distance\ from\ the\ centroid\ of\ the\ bar\ to\ the\ extreme\ compression\ fiber$

, $\rho_h = ratio\ of\ horizontal\ web\ reinforcement$

(10) $\beta_{sc} = \frac{\sigma_{cc}}{f_c'} = \frac{\sigma_{cc,ag} + \sigma_{cc,s}}{f_c'} \leq k_c \beta_{si}$ according to (Laughery & Pujol 2015) $\beta_{si} = 0.85$ known as strut efficiency coefficients of the interface BM shown in figure $\sigma_{cc} = MPa$ effective compressive strength. Diagonal cracks should be included when calculating effective compressive strength σ_{cc}. Shear transfer. The tensile strength of web reinforcement, doweling of longitudinal bars, and the interaction of aggregates are all components of a fractured surface. And

$\sigma_{cc,ag} = aggregates\ interlock,\ effective\ compressive\ strength$,

$\sigma_{cc,s} = sum\ of\ the\ dowel\ action\ bars\ and\ tensile\ strength\ of\ web\ reinforcemen$

(11) $\sigma_\varphi = \sigma_{cc,ag} sin^2\varphi$,(12) $\tau_\varphi = \sigma_{cc,ag} sin\varphi cos\varphi$ since $\varphi = (\alpha - \theta)$ (Vecchio & Collins 1986).

(13) $\tau_\varphi = 0.18\tau_{max} + 1.64\sigma_\varphi - 0.82\frac{\sigma_\varphi^2}{\tau_{max}}$ where τ_φ is the ultimate shear stress while σ_φ is the normal stress. And

(14) $\tau_{max} = \frac{\sqrt{f_c'}}{0.31 + 24w/(a_g + 16)}$ since $a_g = 19\ mm$ is the aggregate size (Bentz 2000) and w is the crack width

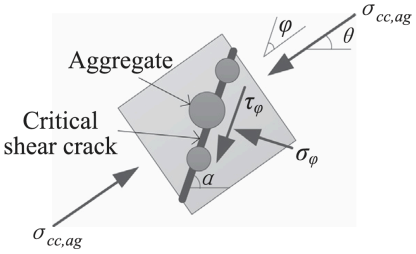

Figure 42 : Interlocking mechanism of aggregates in fine model analysis at CSC

(15) $w = \frac{w_{bond} + w_{de}}{2sin\alpha} = \frac{1.7 s_r \varepsilon_{sc,m} + l_{de}\varepsilon_{sc}}{2sin\alpha}$, (16) $s_r = 2(h - d) + 0.125\frac{\phi_s}{\rho_e}$,

(17) $\varepsilon_{sc,m} = \varepsilon_{sc} - 0.4\frac{f_{ct}}{\rho_e E_s}$

w_{bond} =sliding between longitudinal bars and concrete in a strong bonding location causes crack beneath (Laughery & Pujol 2015) w_{de} =The crack width is created by the slip between longitudinal bars and concrete along the delamination (dowel) fracture (Cavagnis et al. 2015) .$s_r = average\ crack\ spacing$ (Laughery & Pujol 2015). ε_{sc} = strain of longitudinal bars at CSC $\varepsilon_{sc,m}$ = The mean strain of longitudinal bars across the length of s_r,l_{de} =delamination crack length in CSCto the inner edge support plate along the longitudinal bars (18) $\phi_{eq} = \frac{\Sigma n_{s,i}\phi_{s,i}^2}{\Sigma n_{s,i}\phi_{s,i}}$ where $n_{s,i}$ = bar numbers $\phi_{s,i}$ = diameter of reinforcement (19) $\rho_e = \rho\frac{d}{2.5(h-d)}\rho_e$ = reinforcement bar ratio (Taerwe & Matthys 2013). Following the equation (17) the f_{ct} = uniaxial tension strength of concrete:

(20) $f_{ct} = \begin{cases} 0.3(f_c')^{2/3} & for\ f_c' \leq 50\ MPa \\ 1.12(f_c')^{1/3} & for\ f_c' > 50\ MPa \end{cases}$

Solving equation (11) and (12) into (13) obtain the following: (21) $\sigma_{cc,ag} = \zeta\tau_{max}$ where

(22) $\zeta = \frac{-sin\varphi cos\varphi + 1.64sin^2\varphi + \sqrt{(sin\varphi cos\varphi - 1.64sin^2\varphi)^2 + 0.59sin^4\varphi}}{1.64sin^4\varphi}$

when $\varphi, 20^\circ$, $\varphi = 1^\circ - 20^\circ$(23) $\zeta = \frac{8.45}{\varphi - 0.15} + 0.67$, (24) $\varepsilon_{sc} = \eta\varepsilon_{sm}$, where η is the reduction factor the longitudinal bars at the mid span known as the weakest point

(25) $\varepsilon_{sm} = \frac{V_n a(d-c)}{(d-c)^2 E_S \rho bd + [c-(h-d')]^2 E_S \rho' bd' + (d-c)^3 E_S \rho_h b + E_c bc^3/3}$

Where $V_n = applied\ force$, a =shear span of the beam b = width of the beam d = effective depth of the beam $c = depth\ of\ the\ compression\ zone$ E_s = elastic modulus of steel, E_c =Elastic modulus of concrete (26) $(1 - \eta)(T + T_h) = F_{sc,s} cos\theta$ and ρ , ρ' is the ratio of

longitudinal tension and compression bars respectively. ρ_v, ρ_h are the ratio of vertical and horizontal web reinforcement respectively since d' = distance the centroid of the compression bars to the extreme compression fiber. (27) $V_{sc,v} + V_{sc,d} = F_{sc,s} sin\theta$, (28) $\eta = 1 - \frac{V_{sc,v} + V_{sc,d}}{T + T_h} cot\theta$ when $V_{sc,v}$ =shear force carried by vertical crack. $V_{sc,d}$ =shear force of dowel acting on critical shear since forces (29) $T = \varepsilon_{sm} E_S \rho_h (d - c)b \leq f_y \rho_h db$

(30) $T_h = \frac{\varepsilon_{sm} E_S \rho_h (d-c)b}{2} \leq f_{hy}\rho_h(d - c)b$

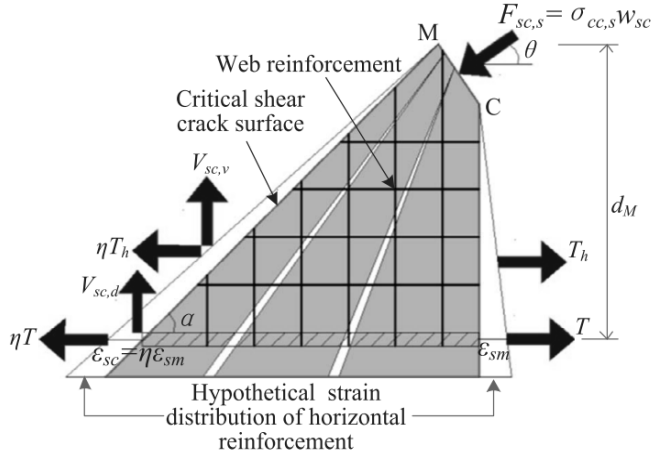

Figure 44: free body diagram of the reinforcement (Chen et al. 2018).

(31) $V_{sc,v} = \frac{\varepsilon_v E_S \rho_h d_M b cot\alpha}{2} \leq f_{vy} \rho_v d_M b cot\alpha$ where $\rho_v =$ ratio of the transverse reinforcement, $\varepsilon_v =$ strain of transverse reinforcement at the bottom of CSC f_{hy} =yield stress of horizontal bars, f_{vy} =yield stress of the vertical reinforcement.

Based on $\varepsilon_{sc} cot^2\alpha = \varepsilon_v$ =transverse reinforcement (Zararis 2003).

$\varepsilon_{sc} = \eta\varepsilon_{sm}$, (32) $V_{sc,v} = \frac{\eta\varepsilon_{sm} E_s \rho_v d_M b cot^3\alpha}{2} \leq f_{vy} \rho_v d_M cot\alpha$,

(33) $V_{sc,d} = (1 - \frac{\sigma_{sc}}{f_y}) \frac{n_s \phi_s^3 f_y}{3 l_{de}}$, $(\sigma_{sc} = \varepsilon_{sc} E_S = \eta\varepsilon_{sm} E_s \leq f_y)$, σ_{sc} known for the tensile stress of the longitudinal bars at the cross section area. The maximum allowable downward force is caused by the interaction of tension force and bending, and the reduction coefficient $1 - \frac{\sigma_{sc}}{f_y}$ allows this. This shows a linear approximation of the reduction coefficient $\sqrt{(1 - \frac{\sigma_{sc}^2}{f_y^2})}$ (Taerwe & Matthys 2013). By substituting the equations above 19, 30 , 32, 33 into 28, assuming $\varepsilon_{sm} E_s = f_y$, (34) $\eta = \frac{-K_1 + K_2 tan\theta}{K_3 - K_1 + K_2 tan\theta}$. Since $K_1 = n_s \phi_s^3 / (3 l_{de})$, $K_2 = \rho bd + \frac{\rho_h b(d-c)}{2}$ and $K_3 = \frac{\rho_v d_M b cot^3\alpha}{2}$, $K_3 = 0$ only if the transverse beam is without transverse reinforcement. $\eta = 1$ when the strain of the longitudinal bars at the critical shear crack is the same at the mid span. $\eta < 1$ when working with a deep beam case verified by (Rogowsky & Macgregor 1983) and (Li et al. 2023). He effective compressive strength can be calculated as (35) $\sigma_{cc,s} = \frac{V_{sc,v} + v_{sc,d}}{b w_{sc} sin\theta}$. In terms of real-world use, the suggested CSTM can be further simplified without resorting to an iterative procedure. It is well established that the shear strength of reinforced concrete beams diminishes as the tensile strain of the longitudinal bars increases, and the longitudinal bars typically remain in the inelastic stage at the point of shear failure.the proposed procedure can take the value of $\beta_{sc} = 0.85$, Therefore, the shear resistance of the RC beams can be conservatively estimated without the need for complex calculations, provided that the longitudinal bars yield. Furthermore, because the shear resistance is not greatly impacted by the effects, the effects of longitudinal bars and transverse reinforcement in compression, as well as the interaction between these two elements in tension, are overlooked $\varepsilon_{sm} = \varepsilon_y$ as $\varepsilon_y =$ yield strain of the longitudinal bar.

(36) $c = (\sqrt{(n\rho)^2 + 2n\rho} - n\rho)d$

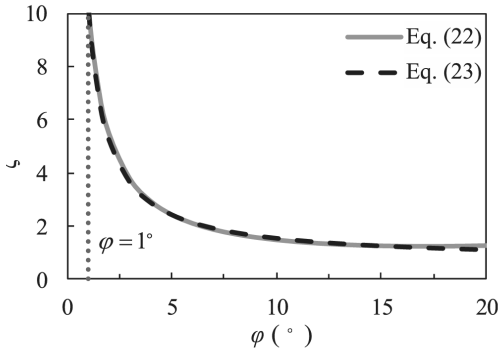

Figure 45: two equations comparison between φ *and* ζ(Chen et al. 2018).

(38) $\sigma_{cc,ag} = \zeta\tau_{max} = \frac{1.33\sqrt{f_c'}}{0.31 + 0.34\alpha\varepsilon_y / sin\alpha}$. The equation (33) states that the shear force caused by the dowel action decreases to zero as the longitudinal bars at CSC reach the yield stage, $d_M = 0.9d$ the effective compressive strength can written as:

(39) $\sigma_{cc,s} = \frac{V_{sc,v}}{b w_{sc} sin\theta} \leq \frac{0.45 f_y \rho_v d cot^3\alpha}{w_{sc} sin\theta} \leq \frac{0.9 d_{vy} \rho_v d cot\alpha}{w_{sc} sin\theta}$,

(40) $V_n = 0.8(F_{si} + F_{sc}) sin\theta$

Failure mechanism of trusses - Non linear analysis

Case of bridge collapse also occurred in the US. On August 1, 2007, the I-35W bridge in Minneapolis, United States, collapsed over the Mississippi River. The failure of a connection at one of the gusset plates is what caused that sudden collapse. The corrosion of the gusset plate and the increased weight on the bridge were potential causes of the collapse of the structure. The failure of steel truss bridge components may result in additional damage or perhaps cause the bridge to collapse. This work presents a non-linear analysis of the failure mechanism of single span and continuous span steel truss bridges utilizing pushover analysis (Astaneh-Asl 2008).

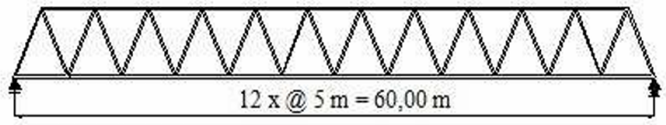

Figure 46: Bridge A1

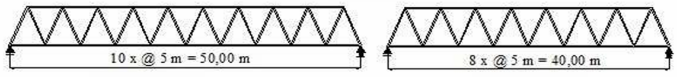

Figure 47: Truss bridge frame side view A2 and A3.

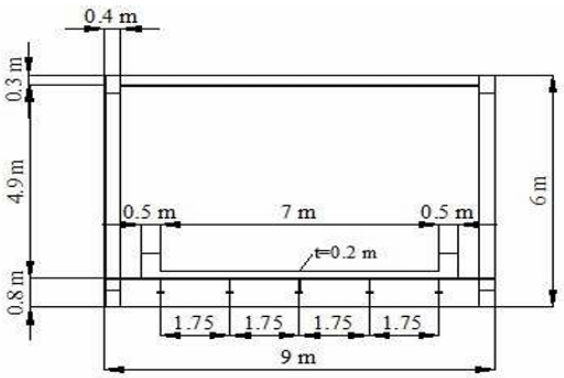

Figure 48: Cross section of bridge dimensions used for structural analysis

The bridge deck is assumed to consist of a reinforced concrete slab with a thickness of 200 mm. The Indonesian industrial standard for steel grades specifies a Young's modulus of 2.1×10^5 MPa, a yield stress of 290 MPa, and an ultimate tensile strength of 500 MPa (Pramana & Darma 2024).

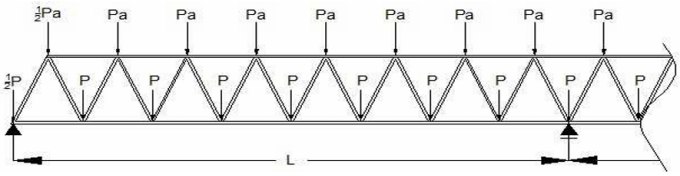

Figure 49: Structural analysis of trusses though pressure distribution (Wahyuni et al. 2016).

Target of displacement of a truss frame

(1) $\delta_T = C_0 C_1 C_2 C_3 S_a (\frac{T_e}{4\pi})^2 g$ (Prestandard 2000)

(2) $S_a = C_D \times S_0 = 0.92 \times 1.2 = 1.104$

As $C_0 =$ *modification factor the spectral and roof displacement* $= 1$

$C_1 =$ *Factor for maximum inelastic displacements* $= 1$ *if* $T_e \geq T_s$,

$C_2 =$ *strength deterioration factor* $= 1$,

$C_3 = 1$ *for structure with positive yield increased displacement factor due to*

$S_a =$ *Response spectrum acceleration*, $T_e =$ *effective period*

(Nugraha et al. 2023).

Model	C_0	C_1	C_2	C_3	S_a	$T_e(s)$	$d_T(cm)$
A1	1	1	1	1	1.104	0.2527	20.19
A2	1	1	1	1	1.104	0.1828	11.03
A3	1	1	1	1	1.104	0.1258	6.96

Table3 : Target of displacement of truss frame results at different models through nonlinear analysis (Wahyuni et al. 2016).

	Base force	(T)	First yield	Ultimate Point	Ductility
Model	First Yield	Ultimate point	$\delta_y(mm)$	$\delta_u(mm)$	$\mu = \frac{\delta_u}{\delta_y}$
A1	133.11	144.07	23.91	25.25	1.06
A2	374.7	387.71	18.06	19.15	1.07
A3	315.22	325.75	12.39	13.23	1.09

Table4 : Comparison of different models results (Wahyuni et al. 2016)

Connections for Sliding Corner Gussets

The beam-column junction opening and closing in braced frames might induce premature rupture of the welded corner gusset connection and/or neighboring framing members.

Previous research has proposed and experimentally studied a sliding gusset connection for buckling-restrained braced frames (BRBFs) to reduce frame action effect. The gusset plate is bolted to beam and column flanges through slotted end plates, allowing sliding at the gusset-to-frame interfaces. To enhance experimental results and create a feasible design approach, high-fidelity finite element models were created and validated against experimental results for sliding gusset connections. A series of numerical parametric studies followed.

Different beam-to-column connection arrangements were examined first. The strengthened beam end created a plastic hinge independent of the gusset connection region, reducing plasticity and strain demands on bolts at the gusset-to-frame interfaces. Second, the comparable tensile force approach was suggested for designing bolts in sliding gusset connections. Different bracing angles and frame member sections were used to quantify the equivalent forces under brace tension action. Thirdly, the sliding gusset connection's behavior was investigated in the context of the combined brace-frame action. The results verified the gusset plate design method and suggested bolt design criteria. Finally, a realistic design approach for the sliding gusset connection in BRBFs was developed based on the results and discussion, making it readily applicable to engineers.

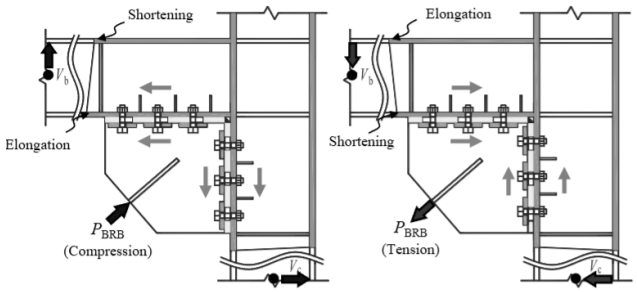

Figure 50: Sliding Gusset Connection (a) assembly of components; (b) relative displacement at the gusset-to-frame interfaces(Zhao et al. 2018).

In their prior study (Zhao et al. 2018), the authors documented full-scale tests of brace-beam-column subassemblies with either a sliding gusset76 connection or a welded connection. This section details the construction of finite element models for the test specimens SC-2 and WC, which represent the sliding gusset connection and the welded gusset connection, respectively. Figure illustrates the test configuration and the finite element model of specimen SC-2.

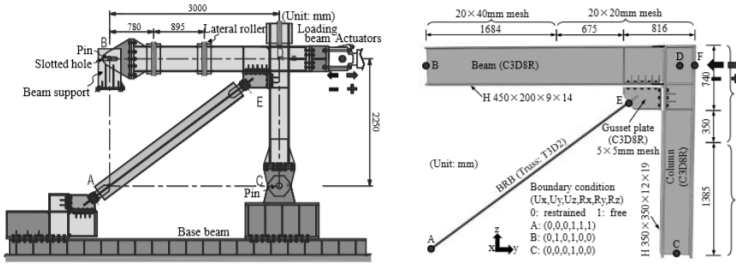

Figure 51 : test set up for structural steel gusset connection set up and FE model (Zhao et al. 2018).

the connections between the gussets. The sensitivity analysis was used to determine the mesh diameters, as depicted in Figure 51. In order to accurately represent the potential deformation behavior, a minimum of three layers of elements were implemented throughout the thickness of each plate. The refined mesh size of 3 mm was employed for the high-strength fasteners in the sliding gusset connection. The 'bolt load' tool in ABAQUS was utilized in order to model the bolt pretension load. The loads that were applied to the bolts at the gusset-to-beam and gusset-to-column interfaces were 140 kN and 257 kN, respectively. The BRB was modeled using a T3D2 truss element, with one end pinned (Point A) and the other kinematically connected to the gusset plate's cruciform cross-section (Point E).

The 'Hard Contact' property was implemented to denote the behavior that is characteristic of all contact surfaces.
To characterize the frictional tangential behavior, the "Coulomb Friction" with "penalty" option was established. The low-frictional butyl rubber layer interface was given a friction coefficient of 0.075 (Chen et al. 2016), while the standard steel-to-steel interface was given a friction coefficient of 0.3. To "tie" together, welded surfaces were modeled. The roller support and the anchored support were implemented at Point B and C in the FE models, respectively, in accordance with the boundary conditions of the test.

(1) $G = E/2(1 + \nu)$ $E = Young's\ modulus, \nu = Poisson's\ ratio$

Category	Material Grade	Young's modulus (GPa)	Yield strength (MPa)	Tensile strength (MPa)	Shear modulus (GPa)	Poisson ratio
Beam Flange	Q235-B	204	237	413	4.08	0.3
Beam Web	Q235-B	204	271	429	4.08	0.3
Column Flange	Q345-B	208	339	507	4.16	0.3
Column web	Q345-B	208	360	514	4.16	0.3
Gusset Plate	Q235-B	205	280	429	4.1	0.28
Flange plate	Q235-B	206	294	426	4.12	0.3
Panel zone plate	Q345-B	206	380	517	4.12	0.3
Stiffener	Q235-B	206	294	426	4.12	0.3
End plate	Q345-B	206	369	517	4.12	0.3
Shim plate	Q235-B	206	294	426	4.12	0.3
Bolt	10.9	206	940	1040	4.12	0.3
Bolt	8.8	206	664	830	4.12	0.3
Sher Stud	N/A	206	294	426	4.12	0.3
Rebar	HRB400	206	400	-	-	0.3

Table 5: Material properties in FE models

E (GPa)	A_{eq} (mm^2)	$f_{y,eq}$ (MPa)	E_t/E	R_0	cR_1	cR_2	a_1	a_2	a_3	a_4
205	2320	262	0.01	20	0.925	0.15	0.052	1.0	0.05	1.0

Table 6: Guiffre-Menegotto-Pinto model parameters of truss element

$E = elastic\ modulus; A_{eq} = equivalent\ cross\ section\ area\ of\ truss$
$E_t = tangent\ modulus f_{y,eq} = equivalent\ yield\ strength\ of\ truss$
$R_0, cR_1\ and\ cR_2 = elastic\ to\ plastic\ branches,\ parameters\ controls,$
$a_1, a_2, a_3 and\ a_4 = parameters\ to\ control\ isotropic\ hardening,$

Concrete slab subassembly with beams and columns

This part modeled and validated the composite beam effect and concrete floor slab. (Lee et al. 2016) created a FE model for the tested beam-to-column assembly with concrete slab, specifically the specimen PN700-C. The beam-to-column connection used welded flange-bolted web arrangement. On the beams, profiled steel decking supported the concrete slab.
The beam has shear studs welded on top. Bi-directional rebars were 50 mm for reinforcement.

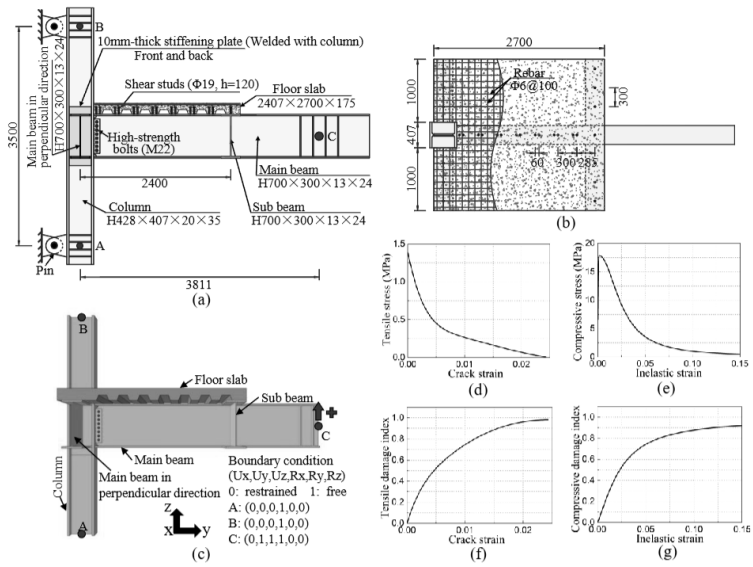

Figure 52 : (Lee et al. 2016) A beam-to-column concrete floor slab connection

(a) Test setup; (b) Floor slab details; (c) FE model; (d) Concrete stress-crack strain relationships; (e) Compressive stress-inelastic strain relationships; (f) Tensile damage-crack strain relationships; (g) Compressive damage-inelastic strain relationships.

'Hard Contact' was delineated to characterize the typical behavior at the contact interfaces. The friction coefficients of 0.4 and 0.3 were established for the tangential frictional behavior at the concrete-to-steel and steel-to-steel contact surfaces, respectively. In order to simplify the process, all of the welded connections were "tied" to each other. It was modeled that the rebars and shear studs would be set into the floor slab. Each bolt was subjected to a pretension force of 220 kN. A pin support was established at the inflection points A and B for the boundary condition. Vertical cyclic loading was applied at point C.

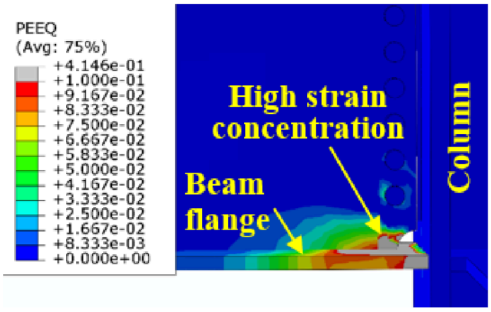

Figure 53: Plastic strain concentration at the boom flange of the beam (Zhao et al. 2018).

The panel zones created according to the P1 criterion exhibited some degree of plasticity, whereas those designed per the P2 criterion remained elastic, demonstrating the efficacy of the P2 criterion in maintaining the elasticity of the panel zone (Liu et al. 2022).

(2) $P1$: $\phi(M_{pb1} + M_{pb2})/V_p \leq \frac{4}{3} f_{vy}$ (3) $V_p = h_{b1} h_{c1} t_p$

(4) $P2$: $(M_{pb1} + M_{pb2})/V_p \leq \frac{4}{3} f_{vy}$ where

$0.75 \leq \phi = moment\ reduction\ factor \leq 0.85$;

$M_{pb1} and\ M_{bp2} = plastic\ moments\ of\ the\ beam\ connecting\ through\ panel\ zone$

$; f_{vy} = nominal\ shear\ yield\ strength\ of\ panel\ zone$;

$V_p = effective\ volume\ of\ the\ panel\ zone$

$h_{b1} = beam\ depth\ measured\ from\ centroids\ of\ beam\ flanges$;

$h_{c1} = column\ depth$; $t_p = panel\ thickness$

The existence of a concrete floor slab was an additional element evaluated in the parametric analysis. In certain variants, a concrete slab measuring 1400 mm in width and 100 mm in thickness was utilized. Bi-directional rebars with a diameter of 8 mm and a spacing of 150 mm were incorporated in the upper layer. Horizontal displacement at point C and B can be followed by the ratio $\frac{d_C}{d_B} = 2$.

Tensile force of the bolt group

An eccentric tensile load is seen as a mixture of a concentric force applied at the geometric centroid of the bolt group, along with a moment about the centroid.

(5) $N_t = \frac{P}{n} + \frac{Pey_1}{\sum_{i=1}^{n} y_i^2}$;

$N_t = critical\ design\ load$;

$P = equivalent\ magnitude\ of\ force$;

$n = total\ number\ of\ bolts$;

$y_i = distance\ of\ bolt\ to\ centroid$;

$i = 1\ for\ critical\ bolt$

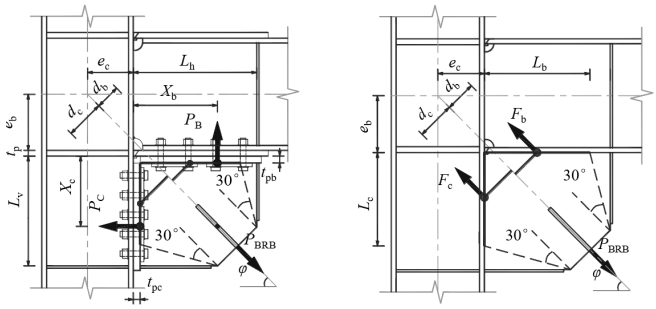

Figure 54: Force analysis for (a) sliding gusset connection, (b) welded gusset connection (Zhao et al. 2018).

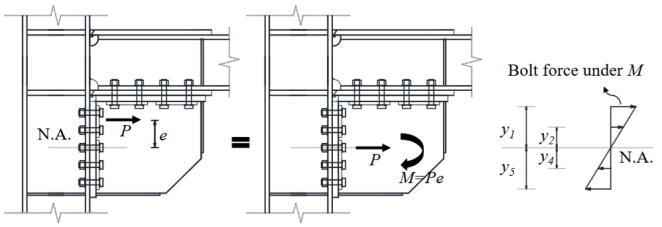

Figure 55: treatment of eccentric load on bold group (Zhao et al. 2018)

(6) $P_B = P_{BRB} sin\varphi$; (7) $P_c = P_{BRB} cos\varphi$; (8) $tan\varphi = \frac{X_c + e_b + t_b}{X_b + e_c}$

$X_b, X_c = distances\ of\ P_b, P_c$

e_b *and* e_c *are half of the beam depth,* t_p $= thickness\ of\ the\ flange,$

$\phi = bracing\ angle\ P_{BRB} = brace\ axial\ force$ Previous research (Cui et al. 2012) revealed a 30° dispersion angle for brace force transmission in welded corner gusset connections, as depicted in Fig. 16(b). In the proposed equivalent force approach, only welds within the dispersion range were considered effective (Lb and Lc). The authors assumed equivalent forces would act at the effective weld centroids parallel to the brace axis, with force values defined by the distances between them (db and dc). (9) $\frac{X_b - t_{pc}}{L_b - t_{pc}} = f(\frac{d_c}{d_b})$, through linear analysis the following can be determined (10) $\frac{X_b - t_{pc}}{L_b - t_{pc}} = 0.3[1 + (\frac{d_c}{d_b})^{0.5}]^{0.6}$,

(11) $X_b = 0.3(L_b - t_{pc})(1 + \sqrt{\frac{d_c}{d_b}})^{0.6} + t_{pc}$, substitute (11) to (8)

(12) $X_c = (e_c + X_b)tan\varphi - (e_b + t_{fp})$

The eccentric equivalent tensile forces were used to calculate the critical bolt design force, Nt, in accordance with the aforementioned equations. Furthermore, the bolt design was constrained to a Nt/P limit of 0.8. The subsequent equations establish the lower bound of the gusset plate dimensions. (13) $L_b = \frac{P_{BRB} cos\varphi}{0.7 t_g f_{vy}}$, (14) $L_c = \frac{P_{BRB} sin\varphi}{0.7 t_g f_{vy}}$ $\varphi = bracing\ angle,$

$t_g = thickness\ of\ gusset\ plate$,

$f_{vy} = nominal\ shear\ yield\ strength\ of\ gusset.$ Using the same demand-capacity ratio based on the cross-section and strength of the welds, a design examination of the welded connection between the gusset plate and end plates is also necessary. (15) $n^b_{bolt} = \frac{P_{BRB} sin\varphi}{0.6 P^b_{bolt}}$,(16) $n^c_{bolt} = \frac{P_{BRB} cos\varphi}{0.6 P^c_{bolt}}$,

n^b_{bolt} *and* $n^c_{bolt} = number\ of\ bolts\ in\ a\ beam\ and\ column,$

P^b_{bolt} *and* $P^c_{bolt} = pretension\ forces$ The arrangement of bolts can be used to modify the size of the gusset plate. To re-evaluate the bolts, (17) $\frac{N^b_t}{P^b_{bolt}} \leq 0.8$,(18) $\frac{N^c_t}{P^c_{bolt}} \leq 0.8$ since

N^b_t *and* $N^c_t = maximum\ tensile\ forces\ carried\ by\ individual\ bolts$

Gusset Design

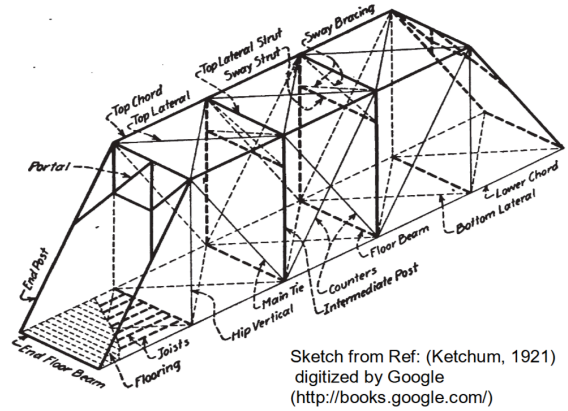

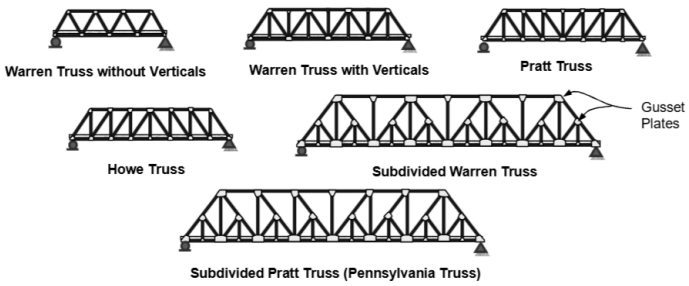

Figure 56: Steel bridge truss frame common types (Astaneh-Asl 1998)

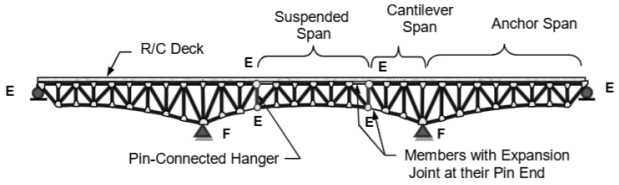

Figure 57: Cantilever warren truss with hanger and suspended Mid-Span (Astaneh-Asl 1998)

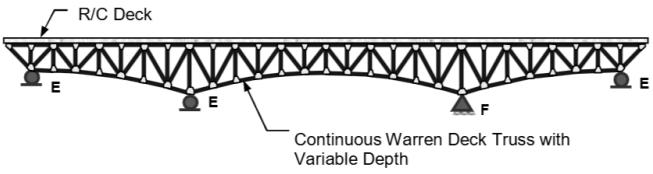

Figure 58: Continuous warren deck truss, E where expansion is allowed F for fixed when expansion is not allowed.

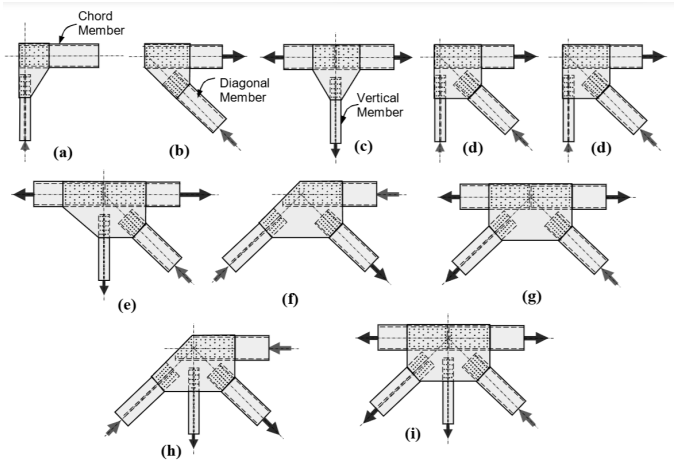

Figure 59: Axial load not necessarily representing the direction of forces for common types of gusset plates in steel bridge trusses(Astaneh-Asl) .

The primary means by which trusses resist bending and shear are the axial strength and rigidity of their members, which are a result of their triangular geometry. The whole behavior of the gusset plates, which are the members and connections of a truss, determines its overall behavior. The failure modes of a truss are identical to those of its members and gusset plate connections. A truss may fail in a global buckling mode as a result of a lack of lateral reinforcement for its compression chord, in addition to the failure of its members and/or connections. This discussion, which is concentrated on the steel truss superstructure of the bridge.

According to research conducted for a conventional truss by (Astaneh-Asl n.d.), inadequate lateral bracing at the truss nodes may lead to buckling of the compression chord and potential out-of-plane displacement of the tension chord due to node instability. The buckling of the compression chord, illustrated in Figure 57, may transpire when the lateral bracing lacks sufficient strength or stiffness to prevent the truss nodes, specifically the gusset plates, from displacing laterally out of plane. The deck structure and the lateral bracing system connect the two parallel main trusses that typically support the gravity load in steel truss bridges. The lateral bracing members serve two primary functions: (a) to function as web members of a horizontal truss, countering horizontal wind and seismic forces, while the chords of the main trusses serve as chord members, and (b) to provide a lateral bracing system for the main trusses, stabilizing the panel points (gusset plates) of these trusses against out-of-plane movement, thereby averting global buckling of the truss chords.

The primary failure modes of a steel truss are enumerated below:
a. Global instability resulting in truss failure
b. Failure of truss components
c. Failure of truss connections, including gusset plates, splices, and supports (e.g., bearings)

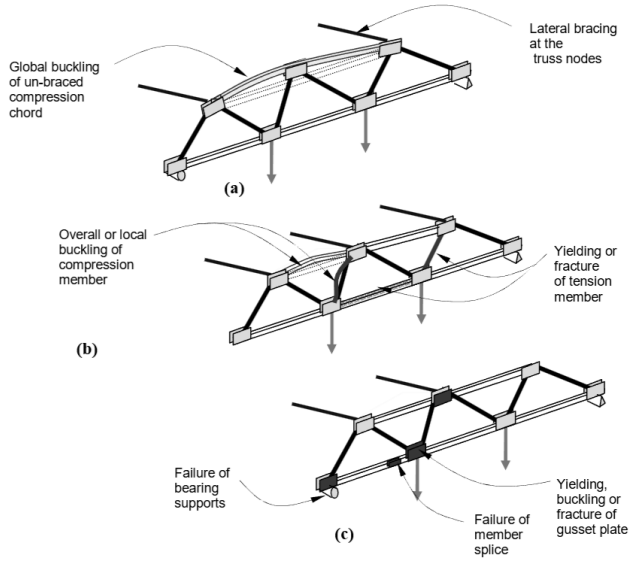

Figure 60: Illustration of failure modes.

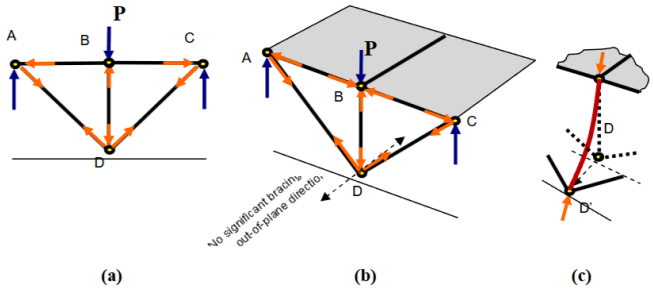

Figure 61: Force reactions inside the structure due to applied load.

To comprehend the reasons for the out-of-plane movement of the tension chord, we will examine the straightforward deck truss depicted in Figure 61 (a). The illustration additionally depicts the axial stresses inside the members, with the bottom chord ADC experiencing tension and the top chord ABC undergoing compression.
At points A, B, and C, the truss joints are stabilized against lateral movement by the deck and its transverse beams. Point D, on the other hand, does not have a brace that would stop it from moving laterally out of the truss's plane. It is evident that member BD is a compressive member. Member BD experiences an increase in axial compression as the applied load P rises. Due to the lack of bracing at point D (Figure 61 (b)), member BD can bend in a rigid body mode, forcing the tension chord ADC out of the plane of the truss and displacing point D to point D′. This phenomena was investigated by (Winter 1960) and subsequently by Yura and his research collaborators (Yura 1995) about the out-of-plane movement of the bottom tension flange of plate girders. To prevent this failure mechanism, Yura presented equations for designing enough lateral bracing. The AISC Specifications now contain the equations (Design 2005).

Design Evaluations

Forces acting on the gusset plate:

Based on (Aashto 1998): (1) $\Sigma n_i Y_i Q_i \leq \phi R_n = R_r$, as (2) $n_i = n_D n_R n_I$ load modifier factor in relation to the component's ductility, redundancy, and operational relevance, as well as the bridge itself Y_i =a load factor that is based on statistics and applied to force effects, Q_i = force effects (e.g., shear, bending moment) in the member. since ϕ = $resistance\ factor$ R_n =The nominal resistance of a component when designing for a specific failure mode. R_r = factor resistance.

For strength limit state ductility

n_D $\geq$ 1.05 for non ductile connection components

$\geq$ 1.00 Ductile strength limits include yielding of gross or holed sections under tension or compression, and critical gusset plate sections under bending moment, axial force, and shear.

= 1.00 for conventional design

$\geq$ 0.95 for components and connections for which additional ductility-enhancing

n_D = 1.0

Strength limit state redundancy

n_R $\geq$ 1.05 for non redundant members

= 1.00 for conventional design r

$\geq$ 0.95 for components and connections for which additional ductility-enhancing

n_R = 1.0

Strength limit state operational

n_I $\geq$ 1.05 for high traffic load

= 1.00 for typical design

$\geq$ 0.95 for lower load

n_I = 1.0

Strength Limit State	n_D	n_R	n_I	$n_i = n_D n_R n_I$
Gross area of steel yield	1	1.05	1.0	1.05
NEt area steel fracture	1.05	1.05	1.0	1.10
Gusset plate buckling	1.05	1.05	1.0	1.10
Block shear failure	1.05	1.05	1.0	1.10
Fracture of rivets, bolts or welds	1.05	1.05	1.0	1.10
Bearing failure of bolts	1.05	1.05	1.0	1.10

Table 7: strength limit state of bolts in a gusset and structural member (Astaneh-Asl)

(3) $(\phi R_n)_{Conn} \geq \left\{ \frac{(\Sigma n_i y_i Q_i)_{member} + n_i (\phi R_n)_{member}}{2} + 0.75 n_i (\phi R_n)_{member} \right\}$, the full strength design recommendation can be written as (4) $(\phi R_n)_{Member} \geq n_i (\phi R_n)_{Member}$.

Failure modes of the gusset connections include:

1. Yield on the gross section under tension
2. Tension-induced fracture in the net section
3. General buckling of compression members
4. Local buckling in compression zones

When a chord member splice is situated within the gusset plate connection, the stresses in the gusset plate may significantly exceed those in instances where the chord member continuously traverses the gusset plates, leading to comparatively minimal forces transmitted to the gusset plate.

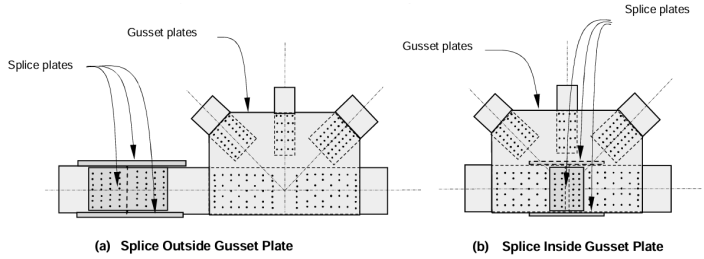

Figure 62: showing location of splice plate (Astaneh-Asl).

Regarding the thickness of gusset plates, the (Aashto 1998) standard specifies a minimum thickness of 9.5 mm . Other literature sources mention a minimum thickness of 12.7 mm. (Bresler & Lin 1960) recommend a gusset plate thickness ranging from 9.5 mm to 12.7 mm for light trusses, and from 15.9 mm to 22.2 mm for heavier trusses, although they do not clarify the criteria for distinguishing between "light" and "heavy" trusses. The provision aims to ensure that the maximum normal stress resulting from the combination of bending and axial normal stresses at any location within the gusset plate does not surpass the yield stress. (5) $\sigma_b = \frac{M}{S_x}$, where M = $(N.mm)$ Bending moment acting on cross section, S_x = mm^3, elastic modulus of the cross section $\sigma_b = N/mm = MPa$ Bending stress. (6) $\tau_{max} < \phi_v F_y/\sqrt{3}$, (7) $\tau_{allow} < (\phi_v)(0.74F_y/\sqrt{3})$ F_y =specified minimum yield stress of steel for the sear area to be the gross area. F_u = specified ultimate strength of steel if the net area is the intended area. $A_n = A_g - A_b$. The length of the unsupported edge of a gusset plate: (8) $L < 2.06(E/F_y)^{1/2} \times t_g$, since $E = MPa$ modulus of elasticity of steel, $F_y = MPa$ specified minimum yield stress of steel and $t_g = mm$ thickness of gusset.

Mechanical performance of high steel plate	HPS 50W, up to 100 mm As-Rolled	HPS 70W up to 100 mm, 50 mm

Yield Strength, $F_y(MPa)$	345	485
Ultimate tensile strength F_u	485	585-760

Table 8: Steel strength mechanical performance (Vermes 2007)

Properties of Steel Riveted bridges	Carbon Steel	Silicon Steel	Nickel Steel
Yield Strength, $F_y(MPa)$	33-36	48-50	48-50
Ultimate tensile strength F_u	60-70	80-95	85-100
Allowable stress in tension F_a	16-18	24-27	27-33

Table 9: Steel strength mechanical performance (Vermes 2007)

Shear failure of the rivets or bolts

(1) $R_r = \phi R_n$, (2)$R_{r-Bolt} = B\phi_{bs}R_{nbs}$ where R_{r-Bolt} =factored shear resistance of bolt group. Σ =number of bolts in group, $\phi_{bs} = 0.8$ resistance factor, R_{nbs} = nominal shear strength of a single bolt in a group connecting the member to the gusset plate. The bolts will slip and bear against the hole wall at a certain point when they are subjected to shear, depending on the degree of pre-tensioning. Friction at the faying surfaces transfers shear until slippage happens. The primary shear transfer mechanism occurs through the bearing compression of the bolt against the hole wall resulting from slippage. In standard civil engineering applications (Aashto 2003), bolts are typically of high strength, and the connected components are occasionally also of high strength.

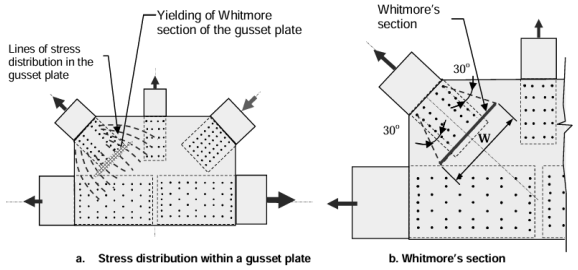

Figure 63: Deformation of the Whitmore section of a gusset plate

Strength limit state check :
(3) $n_i(\phi R_n)Member \leq \phi_y R_{nW}$,since $\phi_y = 0.95$, (4) $R_{nW} = A_{gW}F_y$ know as nominal yield strength (5) $A_{gW} = (W)(t_g)$ for gross area of the gusset since W = width of the whitmore section F_{yg} = specified minimum yield strength of the gusset plate. To create the Whitmore section, as seen in the above figure, two 30-degree lines are drawn from the center of the last bolts to intersect a line that is perpendicular to the member's axis and passes through the first bolt line. The region of the gusset plate situated between the two 30-degree lines is regarded as the gross area of Whitmore's section. The yielding of the Whitmore section of a gusset plate represents the most preferable mode of failure.

Fracture of a whitmore section

If the member force is a tension force, as demonstrated, the Whitmore section's "net area" may fracture.(Bjorhovde & Chakrabarti 1985). The net section of the gusset plate through the last bolt line could become quite weak and this failure mode could become dominant in riveted and bolted bridge gusset plates, particularly with angles connecting the members to the gussets in riveted bridges.

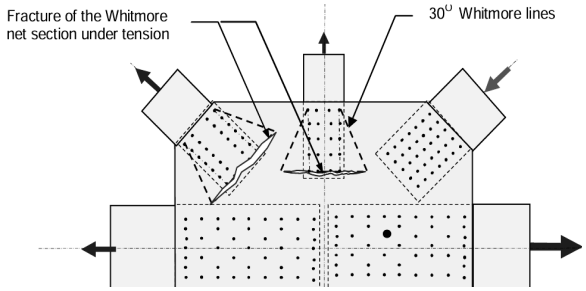

Figure 64: Tension fracture of whitmore gusset.

(1) $n_i(\phi R_n)_{member} \leq \phi R_{nWu}$, $\phi_u = 0.8$ the nominal ultimate strength of section subjected to direct axial tension (2) $R_{nWu} = A_{nW}F_{ug}$, as $A_{nW} = net\ section\ of\ the\ gusset\ plate$ (3) $A_{holes} = \Sigma_{holes}\frac{\pi(d_{bolt}+1.58\,mm)^2}{4}$, The nominal shear strength of the bolt group connecting to the gusset plate: (4) $R_{nbs} = 0.58F_yA_{vg} + F_uA_{tg}$, $F_u\ and\ F_y =$ ultimate stress and yield stress.

Block shear failure of a Gusset

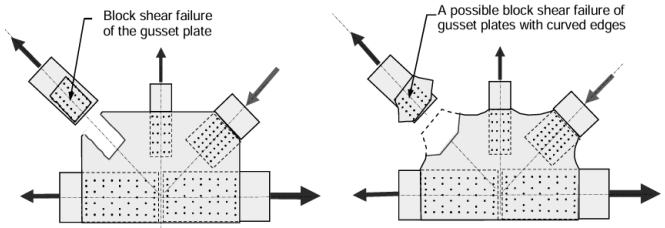

Figure 67: typical black shear failure and incomplete block shear failure

(5) $R_{nbs} = 0.58F_y A_{vg} + F_u A_{tg}$, as $A_{vg} = gross\ area\ in\ shear = (L)(t)$ and $A_{tg} = gross\ area\ in\ tension = (s)(t)$ (Williams & Richard 1996).

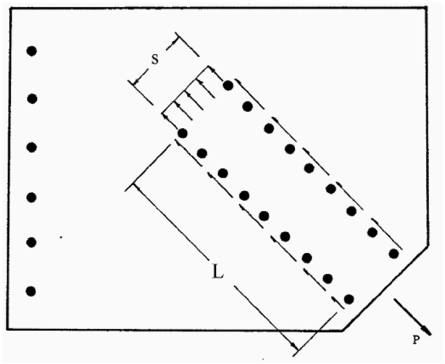

Figure 68: Definition of L and s (Williams 1986).

If (6) $A_{nt} \geq 0.6A_{vn}$: $R_{nbs} = 0.6R_y f_y + F_u A_{tn}$, otherwise (7) $R_{nbs} = 0.6F_u A_{vn} + R_y F_y A_{tg}$

$R_{nbs} = (Pa)$ nominal block shear resistance, A_{vg} = gross area of the plane resisting shear,

A_{tn} = net area along the plane resisting tension stress, A_{vn} = Net area along the plane resisting shear stress, A_{tg} = gross area of the lane resisting tension stress. (Astaneh-Asl et al. 1998).

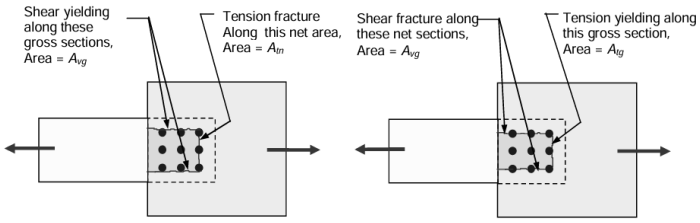

Figure 69 : Failure modes of shear yielding and tension fractures

(8) $R_{nbs} = 0.6F_y A_{vg} + F_u A_{tn}$, (Kulak & Grondin 2001). (9) $n_i(\phi R_n)_{member} \leq \phi_{bs} R_{nbs}$ as $\phi_{bs} = 0.8$, R_{nbs} = the nominal block shear strength pertaining to the axial tension of the gusset plate: if (10) $A_{tn} \geq 0.58A_{vn}$ use (11) $R_r = \phi_{bs}(0.58F_y A_{vg} + F_u A_{tn})$ or (12) $R_r = \phi_{bs}(0.58F_u A_{vn} + F_y A_{tg})$, $F_y = (MPa)$ specified minimum yield strength of the connected material and F_u = minimum tensile strength of the connected materials specified in the following table: $A_{vg} = mm^2$,gross area along the plane resisting shear A_{vn} = net area along the plane resisting shear stress (13) $A_{vn} = A_{vg} - (A_{holes} + \Sigma_{holes}(\frac{s^2}{4g})(t))$.

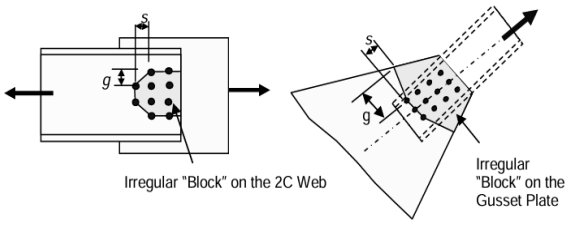

Figure 70: irregular block failure from I section acting on gusset

The application of regulations concerning "staggered" holes in the net area of tension members and the incorporation of the term $(\frac{s^2}{4g})(t)$ not to include in block shear failure scenarios involving inclined "staggered" surfaces that are neither parallel nor perpendicular to the tension line of action.

AASHTO Designation	M 270M Grade 250	M 270M Grade 345	M 270M Grade 345S	M 270M Grade 345W	M 270M Grade HPS 345W	M 270M Grade HPS 485W	M 270M Grades 690/690W	
Equivalent ASTM Designation	A 709M Grade 250	A 709M Grade 345	A 709M Grade 345S	A 709M Grade 345W	A 709M Grade HPS 345W	A 709M Grade HPS 485W	A 709M Grades 690/690W	
Thickness of Plates, mm.	Up to 100 incl.	Up to 100 incl.	Not Applicable	Up to 100 incl.	Up to 100 incl.	Up to 100 incl.	Up to 65 incl.	Over 65 to 100 incl.
Shapes	All Groups	All Groups	All Groups	All Groups	Not Applicable	Not Applicable	Not Applicable	Not Applicable
Minimum Tensile Strength, F_u, MPa	400	450	450	485	485	585	760	690
Specified Minimum Yield Point or Specified Minimum Yield Strength, F_y, MPa	250	345	345	345	345	485	690	620

Table: Minimum mechanical properties of structural steel by shape (Astaneh-Asl).

Consider the block shear fracture path depicted as 'abcdef' in Figure 71. This irregular failure line can be broken down into segments based on their orientation to the applied tensile force:

1. Shear Areas: Segments like 'bc' that run parallel to the tensile force are subjected to shear stress.
2. Tension Areas: Segments such as 'de', which are perpendicular to the tensile force, experience direct tension.
3. Inclined Areas: Segments like 'ab', 'cd', and 'ef' are angled relative to the tensile force and are treated similarly to staggered bolt patterns in net section calculations. These inclined areas are also under tension. When calculating their net area, an additional term,$(s^2/4g)t$, is included for each inclined segment. Here, 's' is the length measured parallel to the tensile force, 'g' is the length perpendicular to it, and 't' represents the thickness of the material.

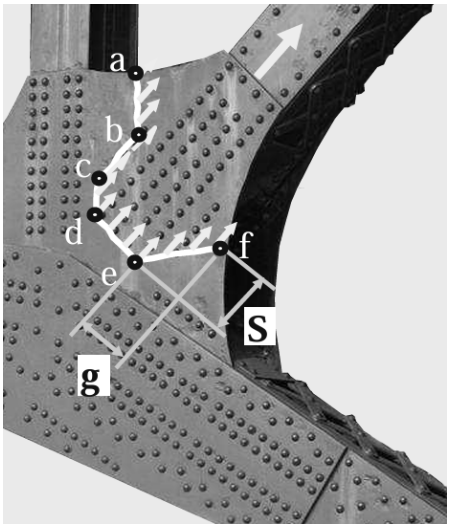

Figure 71: Irregular block shear failure line dimensions

Buckling of Gusset failure

In order to ascertain the buckling capacity of a gusset plate under direct compression (Dowswell 2006), (Astaneh-Asl 1998), one may employ Whitmore's effective width, as illustrated in the accompanying figure. The subsequent equation is proposed for the limit state concerning the buckling of the gusset plate.
This mode of failure is classified as a non-ductile failure mode.

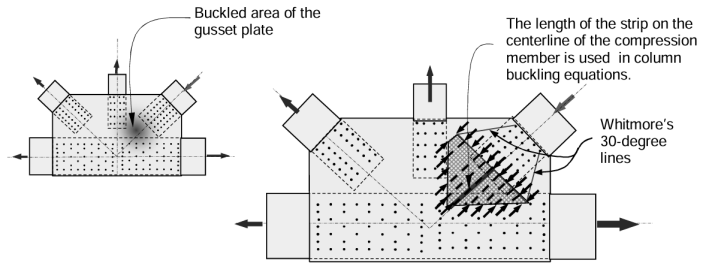

Figure 72 : Gusset plate buckling mechanism

(1) $n_i(\phi R_n)_{member} \leq \phi_c R_{nc}$, since $\phi_c = 0.9$, $R_{nc} =$ *nominal buckling capacity of the gusset* from column equations $R_{nc} = A_{nc} F_y$

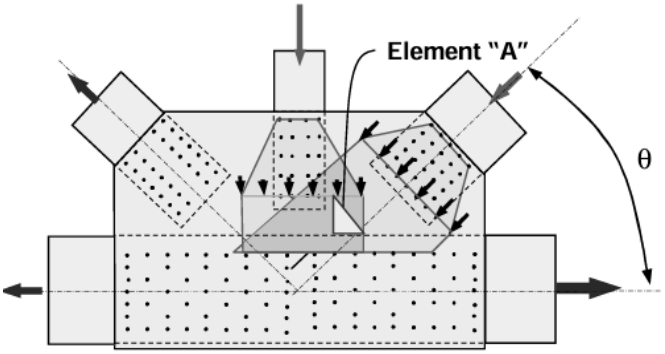

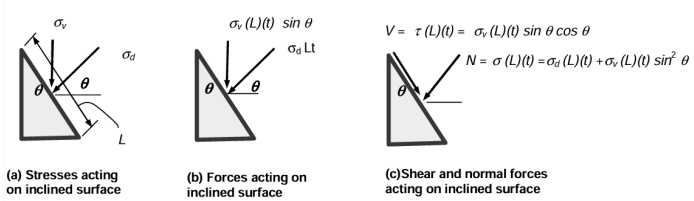

Figure 73 compression areas of the gusset causing buckling, with two adjacent truss members are in compression

The gusset of the vertical element and the horizontal I section of hot-rolled steel are subjected to shear, normal axial forces and stresses.

The following forces are :
(2) $V = \tau(L)(t) = \sigma_v(L)(t) sin\theta cos\theta$,

(3) $N = \sigma(L)(t) = \sigma_d(L)(t) + \sigma_v(L)(t) sin^2\theta$, and for the following stresses can be concluded as: (4) $\tau = \sigma_v sin\theta cos\theta$, (5) $\sigma = \sigma_d + \sigma_v sin^2\theta$. The von Mises criterion can be employed to combine the normal and shear stresses acting on the inclined section. The von Mises stress can then be used as the applied normal stress to be compared to the critical buckling stress of the strip, as shown below: (6) $\sigma_{vM} = \sqrt{\sigma^2 + 3\tau^2}$.

The gusset plate was analyzed using the three methods mentioned above to determine the von Mises stresses at each nodal point, as illustrated in the following figure. First, the normal stress σ and shear stress τ were determined for each node point on the gusset plate in order to establish von Mises stress. Subsequently, these stresses were combined using equation (6). The results of the analysis using the proposed Finite Element Methods (FEM) method are sufficiently accurate for design office applications, whereas the results obtained by applying the Beam Theory are significantly off.

1 $kips$ = 4.45 kN and 1" = 25.4 mm

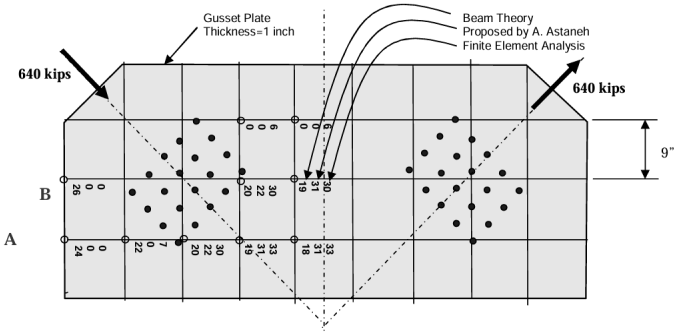

Figure 74: von mises stress in a gusset plate distribution (Astaneh-Asl 2008).

In this case, the gusset plate was analyzed using three methods: (1) the Finite Element Method (FEM), (2) the simplified method

proposed by Astaneh-Asl, and (3) the Beam Theory approach. Figure presents the von Mises stresses calculated at each nodal point using these three methods. As shown in the figure, the von Mises stresses obtained from FEM and the author's simplified method are closely aligned, making both suitable for practical design applications. In contrast, the stresses derived using Beam Theory deviate significantly.

Specifically, the von Mises stresses from the Beam Theory—represented as the third value at each nodal point—are considerably lower than those estimated by FEM (first value) and Astaneh-Asl's method (second value), which better reflect realistic stress conditions. For instance, at Node "C," one of the most highly stressed locations on the gusset plate, the von Mises stresses are 132.3 MPa using FEM, 135.1 MPa using Astaneh-Asl's method, and only 45.5 MPa using the Beam Theory.

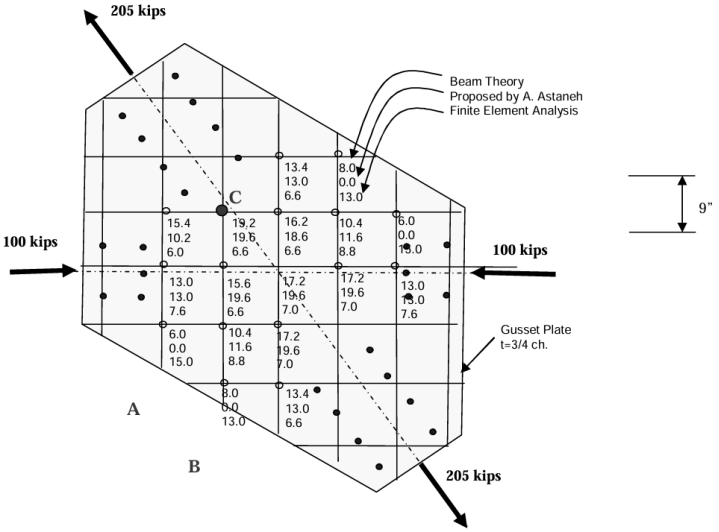

Figure 75: A comparison of von Mises stresses in a bracing system plate in three different methods (Astaneh-Asl).

Buckling of Free Edges of the Gusset Plates

The free edges of the gusset plate may buckle due to the compressive stresses exerted by a compression member connected to the gusset plate. The distinction between edge buckling of gusset plates and buckling of the inner sections remains ambiguous, as does the efficacy of designing a gusset plate for the buckling limit state in preventing edge buckling, a topic extensively summarized by(Chambers & Ernst 2005). Thus, the two buckling modes are examined independently, and both limit states are confirmed. This section primarily focuses on edge buckling.

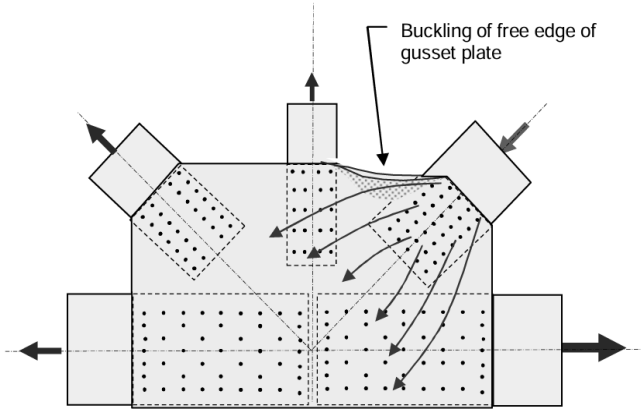

Figure 76: edge buckling of the gusset plate (Astaneh-Asl)

(Aashto 2003) determined that the maximum of unsupported length of a gusset can be expressed as: (1) $\frac{L_{fg}}{t_g} \leq 2.06\sqrt{\frac{E}{f_y}}$, L_{fg} =free length of the gusset calculated for vertical and horizontal , E = modulus of elasticity of steel and $f_y = MPa$ specified minimum yield of steel. While (Vermes 2007) determined the outcomes of compressive gusset plate examinations and evaluations of edge buckling. The study proposed a formula to avert edge buckling before gusset yielding occurs. (2) $\frac{L_{fg}}{t_g} \leq 0.85\sqrt{\frac{E}{F_y}}$.

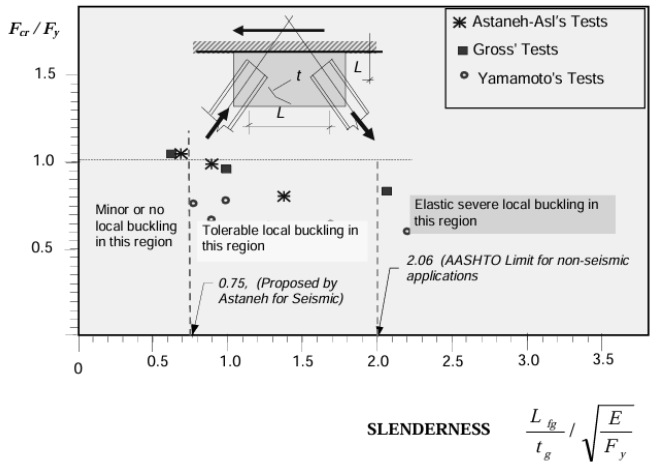

Figure 77: Slenderness comparison through the variation of buckling (Astaneh-Asl 1998).

(Astaneh-Asl n.d.) proposed based on the following test results that the following slenderness should be considered as (3) $\frac{L_{fg}}{t_g} \leq 0.75\sqrt{\frac{E}{F_y}}$.

Yielding of Critical Sections of Gusset Plates in the Presence of Combined Stresses

(Whitmore 1950) tests were designed to determine the actual stresses in the gusset plates and to contrast them with those

determined through beam theory. He concluded that while beam theory reasonably accurately predicted the maximum stresses, it did not accurately predict the location where they occurred.Since the inception of steel truss bridge design, the failure of critical sections of gusset plates has been recognized.The following interaction equation was used to establish normal stresses by linearly adding normal stresses resulting from axial force and bending.The calculation of shear stresses was executed by dividing the shear force exerted on a critical section of the gusset plate by the product of the section's length and its thickness. To put it differently, shear stresses were characterized as "uniform" stresses.

(1) $\sigma_{max} = \frac{N}{Lt} + \frac{Mc}{I} \leq \sigma_{allow}\,(normal\ stress)$, (2)$\tau_{max} = \frac{V}{Lt} \leq \tau_{allow}$

The stress distribution in the critical sections of gusset plates that are subjected to combined loads is not comparable to the stress distribution in beams. In beams, the normal stresses are typically at their highest at the extreme fibers that are distant from the neutral axis, while shear stresses are at their highest on the neutral axis (Goel 1986).

The following interaction equation was used to linearly add the normal stresses due to axial force and bending in order to establish the normal stresses.

The shear stresses were determined by dividing the shear force acting on a critical section of the gusset plate by the length of the section and its thickness. Shear stresses were considered "uniform" in nature.

$\sigma_{max} = MPa = N/mm^2$ Normal stress acting on the critical section of the gusset plate. $N = N$ Axial force acting on the critical section of the gusset $M = kNm$ bending moment $c = mm$ distance from extreme fiber of the gusset plate, $t/2 =$ neutral axis. $I = \frac{tL^3}{12}$ $\tau = MPa$ Shear stress. The von-Mises combined or effective stress is not utilized by (Blodgett 1966). Instead, principal stresses are employed. In machine design, Blodgett's approach is predominantly employed when fatigue is a factor. U.S. standard practice in gusset design does not typically include this feature. In the event that combined stresses are ultimately chosen, the interaction equation from (Neal 1977) (Astaneh-Asl 1998) that employs M, N, and V is the most logical method. (Timoshenko 1955) for each critical element, the principal stress is determined. The maximum principal stress is the greater of the principal stresses acting on critical elements of a critical section of the gusset plate: (3) $\sigma_{1,2} = \frac{\sigma_x + \sigma_y}{2} \pm \sqrt{(\frac{\sigma_x - \sigma_y}{2})^2 + \tau^2}$.

However (Holt & Hartmann 2008) recommended to calculate the principal stresses, two elements on the critical section of the gusset plate are considered to be the critical elements. The two critical elements depicted in Figure below are as follows: (a) Element "A" on the neutral axis, where shear stress is at its highest, and Element "B" on the extreme fiber (i.e. edge) of the gusset plate, where bending stresses are at their highest but shear stress is at its lowest. The "maximum" principal stress acting on the critical section of the gusset plate is subsequently determined by selecting the larger value of principal stress calculated for these two elements.

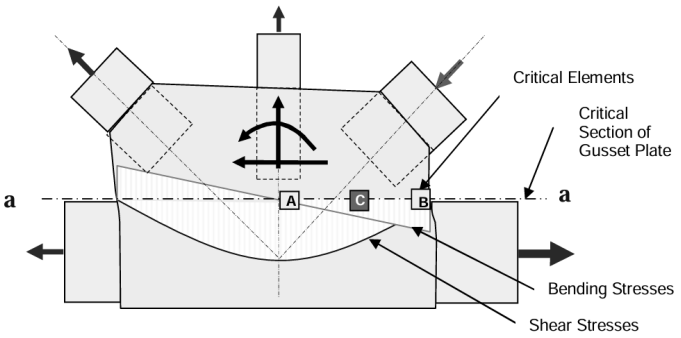

Figure 78: Factors to be evaluated in determining maximum principal stress (Astaneh-Asl).

Gusset plates in bridges cannot be plastified (Imbsen 2009). For trusses subjected to significant seismic forces, such as the stiffening trusses of suspension bridges, dual design criteria are necessary. One criterion, permitting the plastification of the gusset plate as delineated in Equation below, should be employed for seismic design; the alternative criterion, as specified in the current Specifications and further elaborated upon in this section, which prohibits gusset plate plastification, should be utilized for the design of gusset plates under non-seismic loads.

(4) $(\frac{N}{\phi_u N_u})^2 + (\frac{M}{\phi_u M_u})^1 + (\frac{V}{\phi_u V_u})^4 \leq 1.0$

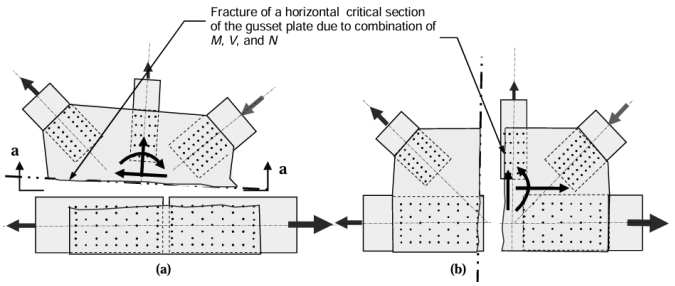

Figure 79: Critical sections of the gusset plate fracture due to the combined forces of shear, axial, and bending moments (Astaneh-Asl).

$since\ \phi = 0.9$, $N =$ Nominal axial force acting on the gusset from the members action load on the bolts of a member $= n_i(\phi R_n)_{member}$, $V =$ shear force acting on gusset , $N_u = A_n F_u$ tensile fracture strength in net area, $M_u = Z_{x-net} F_u$ ultimate moment capacity, $V_u = A_n 0.58 F_u$ ultimate shear capacity and Z_{x-net} =section modulus of the neat area of the critical section of the gusset plate under applied load.

Conclusion

This study integrates fundamental principles, empirical findings, and innovative techniques to enhance safety, durability, and efficiency in modern bridge engineering. Future work should prioritize real-time monitoring, intelligent adjustment systems, and performance-based design methodologies.

Deep beam shear strength was the focus of this investigation. The Cracking Strut-Tie-Model (CSTM) was created by combining the STM concept with experimental and finite element analysis data. Below is a summary of the proposed CSTM's characteristics and benefits.

A building's structural steel model is not subjected to high traffic loads on a suspended foundation, gusset frames are different from those used in buildings, even though they can be used and modeled as an I section. In the design section, the mechanical behavior of bolts in the Rn member is very important because the quantity of drilled bolts affects the section's strength and ability to withstand high torsional stresses; for this reason, plates are used.

Truss Collapse and Gusset Plate Behavior Historical failures like the I-35W bridge collapse underscore the need for robust gusset plate design. This paper analyzes gusset performance under combined stresses and proposes enhancements using FEM and analytical methods. Yielding, buckling, and block shear are assessed using current LRFD guidelines and experimental data.

Structural Optimization and Cable Force Coordination Optimization techniques address both vertical deck deflections and pylon bending moments. Design variables include the number of panels, cable anchor spacing (dx), and erection methodology (temporary supports or cantilever). Proper coordination ensures uniform stress distribution, improving cable longevity and girder efficiency.

Cable-stayed bridge design continues to evolve with advances in material science, computational modeling, and structural analysis. This study integrates fundamental principles, empirical findings, and innovative techniques to enhance safety, durability, and efficiency in modern bridge engineering. Future work should prioritize real-time monitoring, intelligent adjustment systems, and performance-based design methodologies.

Additional research and design analysis are necessary for specific case measurements, as the design for large span bridges with truss frames cannot yet be finalized. The evidence is insufficient to determine whether a truss frame is more suitable for fan-shaped cables or suspension. Additional research is necessary to refine module analysis for individual cable post-tension anchorage connections to the main girder and to optimize for earthquake and wind effects. However, accuracy is contingent upon surveying during construction; the larger the scale, the greater the likelihood of errors, which can excessively stress the damper.

Disclaimer

This report is a research project that has been prepared on behalf of Ahmad Samadi in accordance with the terms and conditions of Building & Infrastructure Pty Ltd (ACN 669 776 845). Engineering Building & Infrastructure cannot be held responsible for any use of, or reliance on its contents by any third party.

The comments and recommendations in this report are derived from our visual observations and our analytical expertise in dealing with similar matters previously. Unless stated otherwise, no invasive enquiries were conducted.

References

Aashto, L., 1998. Bridge design specifications.

Aashto, L., 2003. Manual for condition evaluation and load and resistance factor rating of highway bridges. *American association of state highways transportation officials, DC, Washington*.

Almelda, J.F., 2000. Ultimate limit state of punching in the (fib) FIP recommendationsfor. *Structural concrete*. Available at: https://www.academia.edu/download/90686542/55d92c9e86f564b04285e32a2a3bb7b287ac.pdf.

Anon, Cable-stayed bridges: theory and design. Available at: https://trid.trb.org/View/293478.

Astaneh-Asl, A., *Gusset Plates in Steel BridgesDesign and Evaluation*. researchgate.net. Available at: https://www.researchgate.net/profile/Abolhassan-Astaneh-Asl/publication/345151123_Gusset_Plates_in_Steel_Bridges-_Design_and_Evaluation/links/5f9f5943299bf1b53e59b204/Gusset-Plates-in-Steel-Bridges-Design-and-Evaluation.pdf.

Astaneh-Asl, A., 2008. Progressive collapse of steel truss bridges, the case of i-35w collapse. Available at: http://faculty.ce.berkeley.edu/astaneh/I-35W-webPage/Astaneh-I35W-Keynote-Paper-Steel_Bridges_June-2008-color-Final.pdf.

Astaneh-Asl, A. et al., 1998. Proof-testing of latticed members and their connections on SFOBB. Available at: https://trid.trb.org/View/643319.

Astaneh-Asl, A., 1998. Seismic behavior and design of gusset plates. *Steel tips*. Available at: https://scholar.google.com/citations?user=HNs9mpQAAAAJ&hl=en&oi=sra.

Bentz, E.C., 2000. Sectional analysis of reinforced concrete members [PhD Thesis]. *Toronto: University of Toronto*.

Birrcher, D. et al., 2009. Strength and serviceability design of reinforced concrete deep beams. Available at: https://trid.trb.org/View/891084.

Bjorhovde, R. & Chakrabarti, S.K., 1985. Tests of full-size gusset plate connections. *Journal of structural engineering (New York, N.Y.)*, 111(3), pp.667–684. Available at: http://dx.doi.org/10.1061/(asce)0733-9445(1985)111:3(667).

Blodgett, O.W., 1966. Design of welded structures. *Cleveland: James F.Lincoln Arc Welding Foundation*. Available at:

https://ui.adsabs.harvard.edu/abs/1966dws..book.....B/abstract.

Bresler, B. & Lin, T.Y., 1960. *Design of Steel Structures"*, New York, London: John Wiley &Sons.

Bruer, A., Pircher, H. & Bokan, H., 1999. Computer based optimising of the tensioning of cable-stayed bridges. *IABSE Conference, Malmö*, pp.64–74. Available at: https://www.tdv.at/whitepapers/Cable-StayedBridges/1999_IABSE_Computer%20Based%20Optimising%20of%20the%20Tensioning%20of%20Cable-Stayed%20Bridges.pdf [Accessed February 15, 2025].

Cavagnis, F., Fernández Ruiz, M. & Muttoni, A., 2015. Shear failures in reinforced concrete members without transverse reinforcement: An analysis of the critical shear crack development on the basis of test results. *Engineering structures*, 103, pp.157–173. Available at: https://www.sciencedirect.com/science/article/pii/S0141029615005787.

Chambers, J.J. & Ernst, C.J., 2005. Brace frame gusset plate research phase I literature review. *American Institute of Steel Construction*.

Chen, H., Yi, W.-J. & Hwang, H.-J., 2018. Cracking strut-and-tie model for shear strength evaluation of reinforced concrete deep beams. *Engineering structures*, 163, pp.396–408. Available at: http://dx.doi.org/10.1016/j.engstruct.2018.02.077.

Chen, Q. et al., 2016. Effect of the unbonding materials on the mechanic behavior of all-steel buckling-restrained braces. *Engineering structures*, 111, pp.478–493. Available at: https://www.sciencedirect.com/science/article/pii/S0141029615007944.

Cui, N. & Huang, S., 2019. On the optimal strut-and-tie models and design approach for the cable-pylon anchorage zone. *Journal of civil engineering and management*, 25(6), pp.576–586. Available at: https://journals.vilniustech.lt/index.php/JCEM/article/view/10374.

Cui, Y. et al., 2012. Ultimate strength of gusset plate connections with fillet welds. *Journal of constructional steel research*, 75, pp.104–115. Available at: https://www.sciencedirect.com/science/article/pii/S0143974X12000648.

Design, R.F., 2005. Specification for structural steel buildings.

Dowswell, B., 2006. Effective length factors for gusset plate buckling. *Engineering journal*, 43(2), pp.91–102. Available at: https://ej.aisc.org/index.php/engj/article/view/877.

Ernst, H., 1965. Der E-modul von seilen unter bercksichtigung des durchhanges. *Der Bauingenieur*. Available at: https://cir.nii.ac.jp/crid/1571980074613003776.

Gimsing, N.J. & Georgakis, C.T., 2011. *Cable Supported Bridges: Concept and Design* 3rd ed., Nashville, TN: John Wiley & Sons. Available at: https://books.google.com/books?hl=en&lr=&id=5znYUUUGPZIC&oi=fnd&pg=PP7&dq=Gimsing,+N.%3B+Georgakis,+C.:+Cable+Supported+Bridges,+concept+and+design+(Third+Edition).+John++Wiley+%26+Sons,+Chichester,+UK,+2011.+&ots=6mXZ_lrDoD&sig=0tqkaWukr8JtgHvrw7F-K9m7T88.

Goel, S., 1986. Combined Shear and Tension Stresses. *Journal of Engineering*. Available at: https://ej.aisc.org/index.php/engj/article/view/467.

Hassan, M.M., 2010. Optimum design of cable-stayed bridges. Available at: https://ir.lib.uwo.ca/digitizedtheses/3213/.

Holt, R. & Hartmann, J.L., 2008. Adequacy of the U10 & L11 gusset plate designs for the Minnesota Bridge no. 9340 (I-35W over the Mississippi river).

Imbsen, R.A., 2009. AASHTO guide specifications for LRFD seismic bridge design. Available at: http://www.ce.memphis.edu/7119/pdfs/aashto/2007-03-09guidespec.pdf.

Jin-Keun, K. & Yon-Dong, P., 1994. Shear strength of reinforced high strength concrete beam without web reinforcement. *Magazine of concrete research*, 46(166), pp.7–16. Available at: https://www.icevirtuallibrary.com/doi/abs/10.1680/macr.1994.46.166.7.

Juozapaitis, A. & Norkus, A., 2007. Determination of rational parameters for the advanced structure of a pedestrian suspension steel bridge. *The Baltic Journal of Road and Bridge Engineering*, 2(4), pp.173–181. Available at: https://journals.rtu.lv/index.php/BJRBE/article/view/1822-427X.2007.4.173%E2%80%93181.

Kachurin, V.K., Bragin, A.V. & Erunov, B.G., 1971. Design of suspension and cable-stayed bridges. *Transport*.

Kim, K.-S. & Lee, H.S., 2001. Analysis of target configurations under dead loads for cable-supported bridges. *Computers & structures*, 79(29-30), pp.2681–2692. Available at: https://www.sciencedirect.com/science/article/pii/S0045794901001201.

Kulak, G.L. & Grondin, G.Y., 2001. AISC LRFD rules for block shear in bolted connections—A review. *Engineering journal*, 38(4), pp.199–203. Available at: https://ej.aisc.org/index.php/engj/article/view/763.

Laughery, L. & Pujol, S., 2015. Compressive Strength of Unreinforced Struts. *Aci Structural Journal*, 112(5), pp.617–624. Available at: https://search.ebscohost.com/login.aspx?direct=true&profile=ehost&scope=site&authtype=crawler&jrnl=08893241&AN=109491791&h=Lm4mGvvbpp%2BxTyEOVMjDJ4tWoJAxMmXnKQZutJa8erv4mnPmGNkO5fjlcop6sX8lSCBKtjpevYDWCBrgpebDMw%3D%3D&crl=c.

Lee, C.H. et al., 2016. Investigation of composite slab effect on seismic performance of steel moment connections. *Journal of constructional steel research*, 117, pp.91–100. Available at: https://www.sciencedirect.com/science/article/pii/S0143974X15301164.

Lee, T.-Y., Kim, Y.-H. & Kang, S.-W., 2008. Optimization of tensioning strategy for asymmetric cable-stayed bridge and its effect on construction process. *Structural and multidisciplinary optimization: journal of the International Society for Structural and Multidisciplinary Optimization*, 35(6), pp.623–629. Available at: https://link.springer.com/article/10.1007/s00158-007-0172-9.

Leonhardt, F. & Zellner, W., 1980. Cable-stayed bridges, IABSE Surveys.

Liang, Q.Q. & Steven, G.P., 2002. A performance-based optimization method for topology design of continuum structures with mean compliance constraints. *Computer methods in applied mechanics and engineering*, 191(13-14), pp.1471–1489. Available at:

https://www.sciencedirect.com/science/article/pii/S0045782501003334.

Li, S. et al., 2023. Experimental study of shear performance of high-strength concrete deep beams with longitudinal reinforcement with anchor plate. *Materials*, 16. Available at: https://www.mdpi.com/1996-1944/16/17/6023.

Liu, C. et al., 2022. Seismic fragility estimates of steel diagrid structure with performance-based tests for high-rise buildings. *Journal of building engineering*, 52(104459), p.104459. Available at: https://www.sciencedirect.com/science/article/pii/S2352710222004727.

Lozano-Galant, J. et al., 2012. Construction of cable-stayed bridges built on temporary supports. In *IABSE Congress, Seoul 2012: Innovative Infrastructures – Towards Human Urbanism*. IABSE Congress, Seoul 2012: Innovative Infrastructures - Towards Human Urbanism. Zurich, Switzerland: International Association for Bridge and Structural Engineering (IABSE), pp. 835–841. Available at: https://scholar.google.com/citations?user=XTerT3UAAAAJ&hl=en&oi=sra.

Nazmy, A.S. & Abdel-Ghaffar, A.M., 1990. Three-dimensional nonlinear static analysis of cable-stayed bridges. *Computers & structures*, 34(2), pp.257–271. Available at: https://www.sciencedirect.com/science/article/pii/004579499090369D.

Neal, B.G., 1977. The plastic methods of structural analysis. Available at: https://library.wur.nl/WebQuery/titel/280543.

Nugraha, W. et al., 2023. Developing girder distribution factors in bridge analysis through B-WIM measurements: An empirical study. *Structural Monitoring and Maintenance*, 10(3), pp.207–220. Available at: https://www.researchgate.net/profile/Widi-Nugraha-2/publication/374847687_Developing_girder_distribution_factors_in_bridge_analysis_through_B-WIM_measurements_An_empirical_study/links/65322e5524bbe32d9a537a60/Developing-girder-distribution-factors-in-bridge-analysis-through-B-WIM-measurements-An-empirical-study.pdf.

Pao, Y.-H. & Chen, W.-Q., 2009. Elastodynamic theory of framed structures and reverberation-ray matrix analysis. *Acta mechanica*, 204(1-2), pp.61–79. Available at: https://link.springer.com/article/10.1007/s00707-008-0012-z.

Pramana, R. & Darma, I.S., 2024. Fatigue evaluation of steel truss Arch Bridge based on traffic load simulation using weigh-in-motion data: Case study of Rumpiang Bridge. *Journal of Engineering and Technological Sciences*, 56(6), pp.756–769. Available at: https://jets.itb.ac.id/index.php/jets/article/view/555.

Prestandard, F., 2000. commentary for the seismic rehabilitation of buildings (FEMA356). *Washington, DC: Federal Emergency Management Agency*, 7(2).

Ren, W.-X. & Peng, X.-L., 2005. Baseline finite element modeling of a large span cable-stayed bridge through field ambient vibration tests. *Computers & structures*, 83(8-9), pp.536–550. Available at: https://www.sciencedirect.com/science/article/pii/S004579490400464X.

Rogowsky, D.M. & Macgregor, J.G., 1983. *Shear strength of deep reinforced concrete con tinuous beams*, Edmonton, Alta., Canada.

Straupe, V. & Paeglitis, A., 2013. Analysis of geometrical and mechanical properties of cable-stayed bridge. *Procedia engineering*, 57, pp.1086–1093. Available at: https://www.sciencedirect.com/science/article/pii/S1877705813008709.

Straupe, V. & Paeglitis, A., 2012. Analysis of interaction between the elements in cable-stayed bridge. *The Baltic Journal of Road and Bridge Engineering*, 7(2), pp.84–91. Available at: https://bjrbe-journals.rtu.lv/bjrbe/article/view/bjrbe.2012.12.

Straupe, V. & Paeglitis, A., 2011. Mathematical bases of interaction between elements in cable stayed bridges. , pp.1–8. Available at: https://structurae.net/en/literature/conference-paper/mathematical-bases-of-interaction-between-elements-in-cable-stayed-bridges.

Sung, Y.-C., Chang, D.-W. & Teo, E.-H., 2006. Optimum post-tensioning cable forces of Mau-Lo Hsi cable-stayed bridge. *Engineering structures*, 28(10), pp.1407–1417. Available at: https://www.sciencedirect.com/science/article/pii/S0141029606000484.

Taerwe, L. & Matthys, S., 2013. Fib model code for concrete structures 2010. Available at: https://onlinelibrary.wiley.com/doi/book/10.1002/9783433604090.

Timoshenko, S.P., 1955. STRENGTH OF MATERIALS (PART II) Princeton.

Vecchio, F. & Collins, M., 1986. The modified compression field theory for reinforced concrete elements subjected to shear. *ACI J.*, 83, pp.219–231. Available at: http://www.vectoranalysisgroup.com/journal_publications/jp2.pdf.

Vermes, W.J., 2007. Design and performance of riveted bridge connections. In *Ohio Transportation Engineering Conf*.

Walther, R. et al., 1999. *Cable stayed bridges, 2nd edition*, London, England: Thomas Telford. Available at: https://books.google.com/books?hl=en&lr=&id=AhSgrMcT4sgC&oi=fnd&pg=PA167&dq=walter+et+al.+1999+bridge+&ots=LhjbY4W_21&sig=gK9ZYrWocmp9L0jz2pkwfh5Jghw.

Wang, P.H., Tseng, T.C. & Yang, C.G., 1993. Initial shape of cable-stayed bridges. *Computers & structures*, 47(1), pp.111–123. Available at: https://www.sciencedirect.com/science/article/pii/004579499390284K.

Whitmore, R.E., 1950. Experimental investigation of stresses in gusset plates. Available at: https://trace.tennessee.edu/utk_gradthes/5828/.

Williams, G.C., 1986. Steel Connection Designs Based on Inelastic Finite Element Analyses (GUSSET, BRACING, STRUCTURES). Available at: https://repository.arizona.edu/bitstream/handle/10150/188168/azu_td_8613452_sip1_w.pdf?sequence=6.

Williams, G.C. & Richard, R., 1996. Analysis and design of large diagonal bracing connections. *Structural engineering review*. Available at: https://pascal-francis.inist.fr/vibad/index.php?action=getRecordDetail&idt=3041514.

Winter, G., 1960. Lateral bracing of columns and beams. *Transactions of the American Society of Civil Engineers*, 125(1), pp.807–826. Available at: http://dx.doi.org/10.1061/taceat.0007917.

Wu, B. et al., 2017. Study on finite element model updating in highway bridge static loading test using spatially-distributed optical fiber sensors. *Sensors (Basel, Switzerland)*, 17(7), p.1657. Available at: https://www.mdpi.com/1424-8220/17/7/1657.

Yura, J., 1995. Bracing for stability—state-of-the-art. *Restructuring: America and Beyond*, pp.88–103.

Zararis, P.D., 2003. Shear compression failure in reinforced concreted deep beams. *J Struct Eng*, 129, pp.544–553.

Zhao, J. et al., 2018. Sliding corner gusset connections for improved buckling-restrained braced steel frame seismic performance: Subassemblage tests. *Engineering structures*, 172, pp.644–662. Available at: https://www.sciencedirect.com/science/article/pii/S0141029617324999.